



UNIVERSITÀ
DEGLI STUDI
FIRENZE

SCUOLA DI SCIENZE MATEMATICHE,
FISICHE E NATURALI

CORSO DI LAUREA MAGISTRALE
IN SCIENZE FISICHE E ASTROFISICHE

Towards Strongly Dipolar Superfluids in Two Dimensions

Verso superfluidi fortemente dipolari in due dimensioni

Candidate

Nicolò Antolini (ID number 6062507)

Thesis Advisor

Prof. Giovanni Modugno

Academic Year 2020/2021

Thesis defended on 29 Ottobre 2020
in front of a Board of Examiners composed by:
Prof. Alessandro Cuccoli (chairman)
Prof. Francesco Marin (controrelatore)

Towards Strongly Dipolar Superfluids in Two Dimensions
Tesi di Laurea Magistrale. University of Florence

© 2020 Nicolò Antolini. All rights reserved

This thesis has been typeset by \LaTeX and the UniFiTh class.

Version: August 30, 2021

Author's email: nicolo.antolini@unifi.com

Acknowledgments

Vorrei ringraziare tutto il gruppo di Pisa, Andrea, Carlo, Giovanni, Giulio e Luca, per avermi accolto nel Laboratorio Disprosio durante il periodo di tesi e per tutto quello che mi hanno insegnato. Un ringraziamento a Silvia, per avermi ospitato nel proprio laboratorio durante gli ultimi mesi. Vorrei inoltre ringraziare Giovanni per l'instancabile cura con cui mi ha seguito durante tutto il lavoro e, in particolare, per avermi sempre spronato e motivato nei momenti più difficili.

Contents

Introduction	vii
1 Two-dimensional Dipolar Quantum Gases	1
1.1 Dipolar Bose-Einstein Condensates	1
1.2 Strongly Dipolar Gases	10
1.3 Superfluidity in two dimensions	16
2 Design of a two dimensional system	23
2.1 Experimenting with dysprosium	23
2.2 Optical Dipole Traps and Lattices	24
2.3 Designing the system	28
3 Realization of a one dimensional optical lattice	37
3.1 Assembling a stable laser source	37
3.2 Seed Laser	38
3.3 Fiber Amplifier	44
3.4 Output power stabilization	46
3.5 Building the optical lattice	54
Conclusions	57
A Gaussian beams	59
A.1 Fundamental Mode	59
A.2 Real gaussian beams	61
A.3 Propagation with transfer matrices	63
Bibliography	67

Introduction

Few emotions are as powerful as the one that the experimenter feels when mixing different elements in order to create something new. The spectrum of all the possible outcomes is something we look at with anxiety but, nevertheless, still able to drive our curiosity in pursuing our goals, moving the boundaries one step further. This is what this thesis is all about. Indeed, this work puts the foundations for the experimental realization of a new type of superfluid, based on Bose condensed magnetic molecules with strong dipolar interactions trapped in two dimensions. This system mixes together two main ingredients: the long-range and anisotropic features of dipolar interactions and the possibility to achieve stable molecular gases in two dimensions. In this thesis I analyze these aspects from an experimental perspective, focusing on the design of new tools to effectively move the first steps towards this fascinating goal.

The field of quantum gases started around 25 years ago with the experimental realization of the first Bose-Einstein condensates in 1995 [2, 14]. This achievement opened the way to explore many-body quantum physics phenomena [7] directly linked to the emergence of a macroscopic coherence, typical of Bose condensed systems. One of the frontiers of this field is the study of quantum gases with long-range interactions, which add to the short-range physics a completely new set of phenomena. Perhaps, the most exciting one is the supersolid phase, a novel counter-intuitive state of matter that combines the coherence properties of superfluid with the rigidity of a crystal. Supersolidity has been observed [9, 12, 45] with dipolar quantum gases of magnetic atoms, where the interaction between large magnetic dipole moments provides for long-range, anisotropic interactions [30]. The physics underlying the supersolid phase comes from the interplay between dipole-dipole and van der Waals interactions when they have comparable energies. From this perspective, the real challenge in recent years is the design of strongly dipolar systems, where dipole-dipole interaction dominates and new phenomena are expected. Indeed, when the length associated with dipolar interactions becomes of the same order as the spacing between particles, it would be possible to study the effect of interactions on systems where physics is set by the inter-particle distance. This is the case of Fermi gases, where superfluid effects manifest only when the interaction energy is comparable to the Fermi energy, hence the interaction length is of the same order of $1/k_F$. Fermionic superfluidity has been experimentally investigated together with the observation of BEC-BCS crossover with just van der Waals interactions [52]. From this perspective, the possibility to add strong dipolar interactions to these systems in order to produce exotic fermionic superfluids [4], is really captivating. Moreover new quantum phases are also expected in strongly dipolar gases in optical lattices.

Here the competition of interactions with tunneling between lattice sites could lead to exotic insulating phases with occupation number $1/2$, known as checkerboard insulators [10]. These are the long-range counterpart of standard Mott insulators experimentally observed only with van der Waals interactions. In this case the energy associated to double occupations is greater than the tunneling energy defined by the lattice depth, therefore particles localize and the occupation number is 1. In order to observe checkerboard insulators interaction has to be long range, so that even single occupations of adjacent sites are prevented. These are just a couple of examples of the wide range of fascinating phenomena that would be possible to access with strongly dipolar quantum gases [4, 10, 30].

A possible solution to explore the strongly dipolar regime is to work with electric polar molecules that, in their ground state, exhibit much larger electric dipole moments than their magnetic counterparts. Nevertheless, producing degenerate gases of heteronuclear molecules it is really challenging because direct laser cooling of molecules is hard, and producing ground state molecules starting from quantum gases of atoms is a delicate task [8, 15]. On the other hand, magnetic atoms does not have dipole moments large enough to reach the strongly interacting regime, since density is limited by losses. However, it is possible to produce molecules associating two magnetic atoms, that giving about twice the magnetic moment, make possible to enter an interesting regime for studying strongly interacting systems. Differently from electric molecules, magnetic ones exhibit large dipole moments even in the weakly bound regime [33]. This gives the possibility to produce strongly interacting molecular systems exploiting the very reliable and stable methods developed for magnetic atoms [17], that are currently driving the research in dipolar quantum gases.

In my thesis I went in this direction, building an experimental starting point towards the realization of a quantum gas of dysprosium magnetic molecules. Dysprosium, condensed for the first time in [32], is one of the atom with the largest magnetic dipole moment in the whole periodic table of about $10\mu_B$, and is the same atom used in current experiments about supersolidity [46, 47]. Thanks to its dipolar nature, dysprosium shows also a dense spectrum of Feshbach resonances, that can be exploited to tune its interactions and drive the formation of weakly bound Feshbach molecules. Indeed, controlling an external magnetic field to cross a Feshbach resonance, it is possible to efficiently bring two colliding atoms in a weakly bound molecular state near the free atomic energy threshold. Being in the highest vibrational state, Feshbach molecules quickly decay to lower tightly bound states, gaining a large kinetic energy that produces fast particle losses from the ultracold sample. The inelastic collision at short range responsible for this decay processes are favored by the strong dipolar interactions of the system, and in particular by their attractive part, which plays a huge role in three dimensions. Therefore, in order to have a system with lifetimes long enough to perform experiments, we need to prepare the molecular quantum gas in an external potential that produces a strong confinement in the direction of the magnetic dipoles. This results in a suppression of the attractive part of the dipolar interaction, since the head-to-tail configuration of pairs of dipoles is suppressed, hence in a suppression of the short range collisions [4, 41]. This approach has been demonstrated in [17], where a thermal gas of weakly bound molecules of erbium

showed a lifetime of tens of ms. Differently from the latter case, my work aims at exploring the superfluid regime with this strongly dipolar systems. While condensation of two-dimensional gas with contact interactions has been extensively studied [22], only marginal research has been done in the dipolar case [37]. In two dimensions the quantum phase transition leading to superfluidity is intrinsically different from the standard Bose-Einstein condensation happening in a three-dimensional gas. The phenomenon is described by the Berezinskii-Kosterlitz-Thouless theory [28], which predicts superfluidity in interacting Bose gases below a critical temperature that is directly proportional to the two-dimensional density of the system [22]. Intuitively, also the loss rates for inelastic collisions are proportional to the density [41], therefore high critical temperatures mean shorter lifetimes for the system. Moreover, density is directly linked to the confining optical potentials we use in experiments. In this work I analyze this problem, translating it to the case of dysprosium molecules and finding the most promising parameters to aim for in experiments. In particular, I use theoretical models for the Berezinskii-Kosterlitz-Thouless critical temperature and molecules loss rate to estimate the system target density and temperature and design a trapping potential giving lifetimes of about 100 ms. This is a one dimensional optical lattice where single lattice sites, separated by 532 nm, can be described as well isolated disks. The trap frequency along the lattice direction is much larger than the transverse one, therefore the system trapped in each lattice site acts in a quasi-two dimensional system. As a pure experimental part of this work, I also realized a suitable laser source to build this new one-dimensional lattice, which I also designed and realized experimentally.

The thesis is organized as follows.

In Chapter 1 I summarize all the different theoretical aspects involved. I start by reviewing dipolar interactions, discussing their role in quantum gases experiments and the interesting effects leading to supersolidity. Then I move to strongly dipolar systems, focusing on the case of magnetic molecules. In particular, I intuitively present the mechanism used to produce weakly bound Feshbach molecules and the theoretical model to study their stability in two dimensions. In the final part of the chapter I also present the phenomenology of superfluids in 2D, introducing the basic bricks of Berezinskii-Kosterlitz-Thouless transition, connecting it also to the dipolar case.

Chapter 2 is devoted to the design of the experiment for the realization of a strongly dipolar superfluid in two dimensions. Here I first summarize the experimental set up currently used in the group of G. Modugno in Pisa, in order to frame the upcoming experiment and present the main features of dysprosium. I also review the basics about optical trapping methods, focusing on optical lattices and discussing heating rates. At this point, having presented all the theoretical ingredients, I present the simulations of the system parameters, analyzing the interplay of the different effects linked by the system density, and ultimately by the trapping frequencies.

In Chapter 3 I present the experimental realization of a new stable laser source with high power and the design of the one-dimensional lattice needed to produce a 2D dipolar superfluid.

Chapter 1

Two-dimensional Dipolar Quantum Gases

In this Chapter I present the main theoretical aspects involved in the physics of dipolar quantum gases and superfluids in two dimensions, which constitutes the object of this thesis. In Section 1.1 I start with dipole-dipole interaction, focusing on how it modifies the physics of non-dipolar superfluids, adding a new interaction mechanism to these systems. I also discuss the system excitations and instabilities, showing how dipolar quantum gases can be exploited to study new phenomena, like the recently observed supersolid phase. In Section 1.2 I move to the case of strongly dipolar systems, which can be realized exploiting weakly bound magnetic molecules. I discuss the formation mechanism of these molecules, starting from an atomic Bose-Einstein condensate of magnetic atoms, and the stability of the molecular system against losses. In the final part of this Chapter, in Section 1.3, I summarize the theory of Bose-Einstein condensation in 2D and the main theoretical results of Berezinskii-Kosterlitz-Thouless theory, which describes the superfluid transition in two-dimensional systems.

1.1 Dipolar Bose-Einstein Condensates

Interactions in a dipolar quantum gas

Considering an ensemble of N unpolarized dipoles in free space, the dipole-dipole interaction (DDI) between two of them, with polarization vectors \mathbf{e}_1 and \mathbf{e}_2 and relative position \mathbf{r} , is

$$U_{dd}(\mathbf{r}) = \frac{D^2}{4\pi} \frac{(\mathbf{e}_1 \cdot \mathbf{e}_2) |\mathbf{r}|^2 - 3(\mathbf{e}_1 \cdot \mathbf{r})(\mathbf{e}_2 \cdot \mathbf{r})}{|\mathbf{r}|^5}. \quad (1.1)$$

The strength of the interaction depends quadratically on the dipole moment D , with D^2 equal to $\mu^2 \mu_0$ (d^2/ϵ_0) for magnetic (electric) dipoles, where μ (d) is the magnetic (electric) dipole moment of the particles and $\mu_0 = 4\pi \times 10^{-7} \text{ H/m}$ ($\epsilon_0 = 8.85 \times 10^{-12} \text{ F/m}$) the vacuum permeability (permittivity).

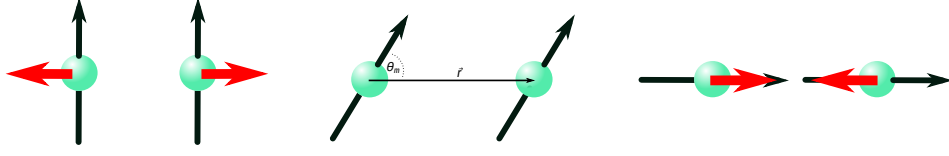


Figure 1.1. Dipole-dipole interactions in a polarized sample. When two dipoles are sitting side-by-side (left) they experience a repulsive potential $D^2/(4\pi r^3)$. In the other extreme case, where they are in head-to-tail configuration they instead attract each other, with a potential $-2D^2/(4\pi r^3)$. At the angle θ_m (center) we have non interacting dipoles.

The expression of U_{dd} in Eq. 1.1 become simpler for a polarized sample, which is always the case in quantum gases experiments, where an external field defines the polarization axis of the system. Indeed, the DDI is in this case

$$U_{dd}(r, \theta) = \frac{D^2}{4\pi} \frac{(1 - 3 \cos^2 \theta)}{r^3} \quad (1.2)$$

where θ is the angle between \mathbf{r} and the polarization axis. As one can clearly see from Eq. 1.2, U_{dd} has a r^{-3} tail responsible for its long-range character and is strongly anisotropic. Indeed, changing θ (i.e. the external polarizing field) not only changes the strength of U_{dd} , but also the interaction nature itself. While dipoles *side-by-side* ($\theta = \pi/2$) repels each other, when they are in *head-to-tail* ($\theta = 0$) configuration the interaction is attractive, with twice the strength. As sketched in Fig. 1.1, for the *magic angle* $\theta_m = \cos^{-1}(1/\sqrt{3})$ repulsive and attractive dipole forces cancel each other. This dependence on the dipoles orientation, can be in principle exploited to tune the DDI [19] in ultra-cold atoms experiments.

Another important feature of dipolar interaction is its long-range nature. Indeed, a central potential $U(r) \sim 1/r^\gamma$ is short-range in \mathcal{D} dimensions, when meets the condition

$$\int_{a_0}^{+\infty} \frac{1}{r^\gamma} r^{\mathcal{D}-1} dr < \infty \quad (1.3)$$

where a_0 is an arbitrary cut-off preventing divergence in $r = 0$. When $\mathcal{D} - \gamma < 0$ the integral in Eq. 1.3 (proportional to the interaction energy) converges, meaning that particles infinitely distant do not interact. In the dipolar case ($\gamma = 3$) this condition holds only for $\mathcal{D} = 1, 2$, where U_{dd} has finite range, while in three dimensions it is not satisfied, leading to a long-range behavior.

In a dipolar BEC we have to take into account DDI together with van der Waals interactions, which typically dominate in a dilute system of neutral atoms. Differently from U_{dd} , this is a short-range, isotropic interaction that can be described by the Lennard-Jones potential

$$U_{LJ}(r) = 4\epsilon \left[\frac{C_{12}}{r^{12}} - \frac{C_6}{r^6} \right]. \quad (1.4)$$

However, at low energies the van der Waals interaction is described by a single parameter, a_s , that is the s-wave scattering length of the two-body problem. Therefore, the Lennard-Jones potential can be replaced by a contact *pseudopotential* U_{vdW} with

constant Fourier transform $g = 4\pi\hbar^2 a_s/m$ which gives the same scattering length of U_{LJ} [25]:

$$U_{vdW}(r) = g \delta(r) \quad (1.5)$$

where $\delta(r)$ is the Dirac δ function. In ultracold non dipolar atoms experiments, where temperatures are typically under 1 μ K, this description is in practice always valid. A similar result cannot be applied instead, to the dipolar case, where all partial waves contribute even at very low energies, due to the long-range tail of the interaction [30]. Nevertheless, it is useful to rescale the U_{dd} coupling constant $D^2/(4\pi)$, defining the dipolar length

$$a_{dd} = \frac{D^2 m}{12\pi\hbar^2} . \quad (1.6)$$

At this point, to quantify the interplay between dipolar and contact interaction, we can define the dimensionless parameter

$$\epsilon_{dd} = \frac{a_{dd}}{a_s} = \frac{D^2}{3g} \quad (1.7)$$

that can be tuned in experiments exploiting a Feshbach resonance [11] to modify the scattering length a_s .

The atomic species we consider in this work is dysprosium. The details about the experimental set up used for the cooling and trapping of this atom will be discussed in Chapter 2, while here we present briefly its main features as a dipolar atom. With $\mu \sim 9.93\mu_B$, dysprosium is the atom with the largest magnetic dipole moment, after holmium (which however has not been condensed yet [35]), in the whole periodic table. This is quite impressive if compared to the dipole moment of alkali atoms, that are of the order of one Bohr magneton [48]. For this reason, dysprosium has by nature a long dipolar length a_{dd} of about 130 a_0 which is comparable to its s-wave scattering length a_s . As we will see in the next section, a_s can be tuned around its background value $a_{bg} \sim 140 a_0$, allowing ϵ_{dd} to span from less than 1 to almost 1.5, making possible to observe novel phenomena emerging in dipolar superfluids.

Feshbach resonances

Starting from a phenomenological point of view, we can say that Feshbach resonances are in practice singularities in the scattering length of contact interactions, occurring for particular values of the external magnetic field. Around these resonances, the s-wave scattering length is described by

$$a_s(B) = a_{bg} \left[1 - \frac{\Delta}{B - B_0} \right] \quad (1.8)$$

where B_0 and Δ are the resonance location and width, while a_{bg} is the value of a_s far from B_0 [11]. In particular, we see from Fig. 1.2 that a_s diverges at B_0 changing sign across the resonance. The basic explanation of the physics behind this phenomenon can be understood thinking about a simple problem in quantum mechanics: the

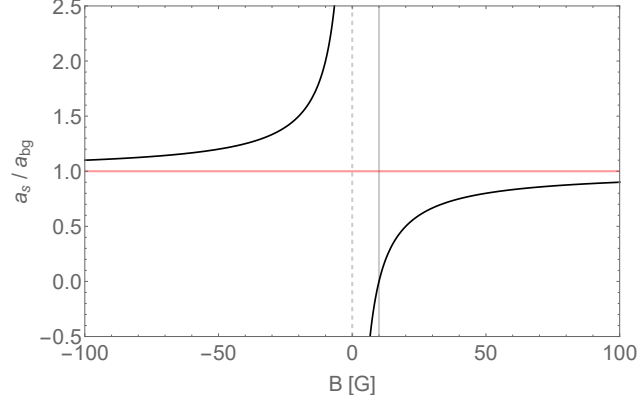


Figure 1.2. Scattering length a_s across a Feshbach resonance. The vertical dashed line indicates the resonance location $B_0 = 0$ G; the zero-crossing is highlighted by the vertical gray line at $\Delta = 10$ G which is also the resonance width; the horizontal red line marks the background scattering length.

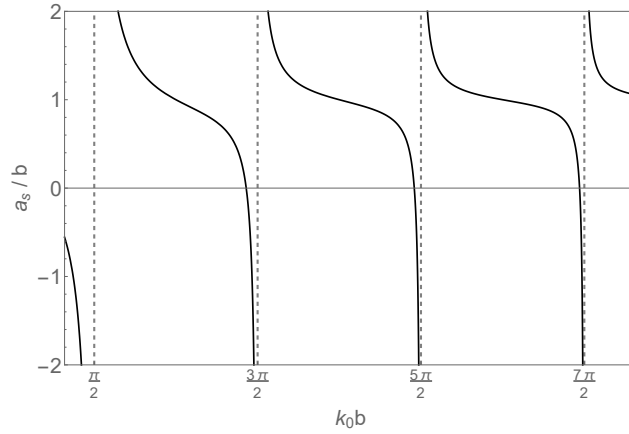


Figure 1.3. Scattering length a_s for particles in a square-well scattering potential [39]. Here $k_0^2 = 2mV_0/\hbar^2$ and b is the range of the well. Each divergence marks a new bound state in the system while increasing the depth of the potential.

scattering in a square-well potential. Taking a potential $V(r) = -V_0$ for $r < b$ and zero elsewhere, we can solve the two-body s-wave scattering problem obtaining

$$a_s = b \left[1 - \frac{\tan(k_0 b)}{k_0 b} \right] \quad (1.9)$$

with $k_0^2 = 2mV_0/\hbar^2$ being the characteristic k associated to the $V(r)$. As we can see in Fig. 1.3, in this case a_s diverges each time $k_0 b = (2n + 1)\pi/2$, meaning that for particular shapes of $V(r)$ (depth and range) something happens that strongly affects the scattering length. Indeed, looking for the energy of weakly bound states (with $|E_b| \ll V_0$) we find $E_b \sim 1/a_s^2$, suggesting that a new bound state *enters the well* every time a_s diverges. This conceptual result holds also for two-body potentials more complex than the square-well, as in the case of interacting ultracold atoms.

Resonances broad enough to have a good control over a_s , can be exploited to tune contact interactions, passing for example from weakly to strongly interacting regime, or realizing non-interacting systems resembling ideal gases of bosons or fermions [11]. This can be done by tuning the interactions around the zero-crossing magnetic field, defined from Eq. 1.8 as

$$B_{ZC} = B_0 + \Delta. \quad (1.10)$$

Feshbach resonances can also be used to change sign to a_s , exploring the collapsing dynamics of trapped gases [39], where attractive interactions cause significant losses. This provides also a natural method to locate resonances, by measuring the number of atoms at different values of magnetic field: the Feshbach spectrum can be mapped with atom-loss spectroscopy. As we will see later in this chapter, Feshbach resonances can be exploited also to produce ultracold weakly bound molecules starting from atomic samples. For these reasons, Feshbach resonances are perhaps one of the most important experimental tools in the field of quantum gases.

To better understand the analogy with the square-well and also grasp the subtle differences of the Feshbach resonance case, we consider two molecular potentials like the ones in Fig. 1.4 (left). Considering two atoms far from each other with energy E_O slightly above zero, the low lying curve represents an open channel for their scattering, while the other one is energetically not accessible, hence corresponds to a closed channel. The idea is that when a bound state with energy E_C in the closed channel approaches E_O , a Feshbach resonance occurs and a_s become infinitely large [11], as in the case of the square-well potential. Note that in that case the potential must be modified (increasing its depth or range) in order to host a new bound state, while here two different potentials are involved and it is possible to change their energy difference, i.e. $(E_C - E_O)$, acting on an external parameter. Indeed, the bound state in the closed channel and the scattering state in the open one have in general two different magnetic moments hence, in presence of an external magnetic field, they have a non zero relative Zeeman energy shift. Therefore, by changing B we change $(E_C - E_O)$ eventually crossing the resonance, where a_s changes accordingly to Eq. 1.8, as we mentioned.

It must be pointed out that the two-channel model of the Feshbach resonances [13] we sketched above constitutes a zero-order explanations of what happens with alkali

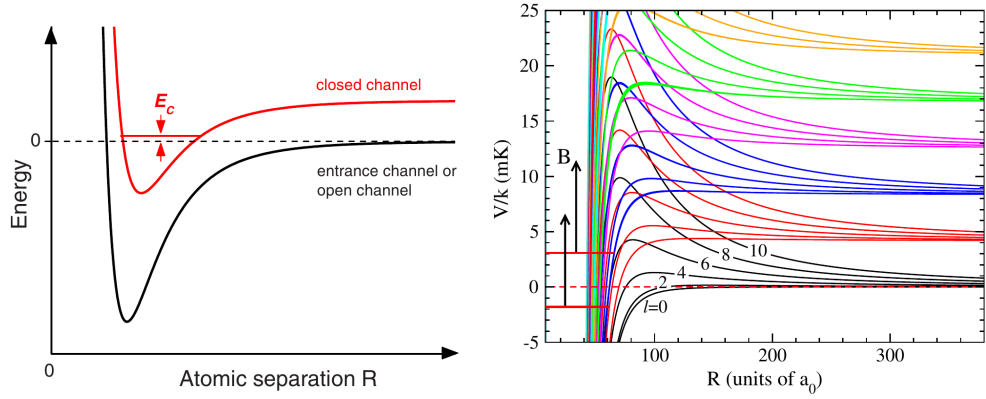


Figure 1.4. Open and closed channels in Feshbach resonances. Differently from the simple two-channel resonance (left) in the dipolar case (right) a great number of channels are involved. In the left plot, adapted from [11], E_C is the energy of the bound state closest to E_O . The plot on the right shows 91 channels for $^{164}\text{Dy} + ^{164}\text{Dy}$ scattering, calculated in [40].

atoms, where molecular potentials are isotropic and only s-wave scattering processes can be considered. Indeed, when the scattering potential depends only on the magnitude of the inter-atomic distance it is possible to label a certain Feshbach resonance with its own partial wave, since different partial waves are not coupled. On the other hand, with dipolar atoms, anisotropic effects in interactions become important and molecular potentials associated to many different partial waves are mixed together [29, 40]. As an example, consider Fig. 1.4 (right), where a great number of molecular potentials contributes to the global scattering problem. As a consequence, the Feshbach spectrum of dipolar atoms is very dense [34], as one can see from Fig. 1.5 where an impressive number of resonances populate a broad region of magnetic field.

In experiments with dipolar BECs the role of Feshbach resonances is even more important, since tuning a_s directly change the *dipolarity* of the system modifying ϵ_{dd} [30]. As we will see in the next sections, exploring the $\epsilon_{dd} > 1$ regime is extremely interesting because of the many effects that stem from DDIs, such as the emergence of a roton minimum [38] in the spectrum that lead dipolar BECs to share some similarities with another bosonic quantum fluid: liquid helium.

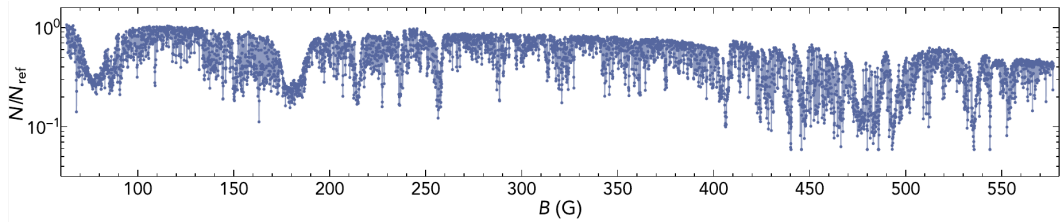


Figure 1.5. Feshbach spectrum of ^{164}Dy ($J = 8$, $m_J = -8$) mapped through the atom-losses measured in [34] for a broad region of the external magnetic field at $T = 2.4 \mu\text{K}$.

Excitation spectrum and instabilities

At the mean field level we can study a dipolar condensate generalizing the Gross-Pitaevskii Equation (GPE) that describes the dynamic of standard BECs, including the DDI term. This leads to the following non-linear equation for the condensate wave function $\phi(\mathbf{r}, t)$ [39]:

$$i\hbar \frac{\partial \phi(\mathbf{r}, t)}{\partial t} = \left[-\frac{\hbar^2 \nabla^2}{2m} + U_{\text{trap}}(\mathbf{r}) + g|\phi(\mathbf{r}, t)|^2 + \Phi_{dd}(\mathbf{r}, t) \right] \phi(\mathbf{r}, t) . \quad (1.11)$$

Note that, while contact interaction energy depends on the density $|\phi(\mathbf{r}, t)|^2$ at a given position, the dipolar term

$$\Phi_{dd}(\mathbf{r}, t) = \int U_{dd}(\mathbf{r} - \mathbf{r}') |\phi(\mathbf{r}', t)|^2 d\mathbf{r}' \quad (1.12)$$

is non-local due to its long-range nature. For a homogeneous gas $|\phi(\mathbf{r}', t)|^2 = n_0$ is constant and Φ_{dd} is simply the product of density n_0 times the Fourier transform of U_{dd} , which can be calculated [42] starting from Eq.1.2:

$$\tilde{U}_{dd}(\mathbf{k}) = D^2 \left(\cos^2 \theta_k - \frac{1}{3} \right) . \quad (1.13)$$

Not surprisingly, the characteristic anisotropy of DDI manifests also in the reciprocal space through the dependence on θ_k , that is the angle between \mathbf{k} and the polarization axis. The homogeneous case (namely $n_0 = \text{const}$, $U_{\text{trap}} = 0$) is interesting mainly because we can directly calculate the excitation spectrum of the condensate from Eq.1.11. For density perturbations with wave vector \mathbf{k} , the small oscillations frequency is given by

$$\omega(k) = k \sqrt{\frac{n_0}{m} \left(g + \tilde{U}_{dd} \right) + \frac{\hbar^2 k^2}{4m^2}} \quad (1.14)$$

that shows a phonon-like dispersion for small k , with sound velocity modified by the DDI. When $\epsilon_{dd} > 1$, the anisotropic term \tilde{U}_{dd} could lead to a phonon instability characterized by imaginary excitation frequencies for $k \rightarrow 0$. Caused by the attractive part of U_{dd} , this phonon instability is favored for perturbations with \mathbf{k} orthogonal to the polarization axis ($\theta_k = \pi/2$), that produce high density zones where dipole are in head-to-tail configuration.

A different kind of instability appears when we consider trapped systems. Indeed, confining potentials add a specific length scale to the system that modifies Eq. 1.13 giving an explicit k dependence to the interaction. In elongated harmonic traps this length scale is the harmonic oscillator length ℓ along the strong trap axis. This changes the homogeneous case spectrum in Eq. 1.14 leading the appearance of a maximum and a minimum around $k_{\text{rot}} \sim 1/\ell$ that resembles the maxon-roton spectrum in superfluid helium. While in helium the roton gap can be changed only through a change of the density (the pressure), a remarkable feature of dipolar quantum gases is the possibility to tune the gap in various ways, including through

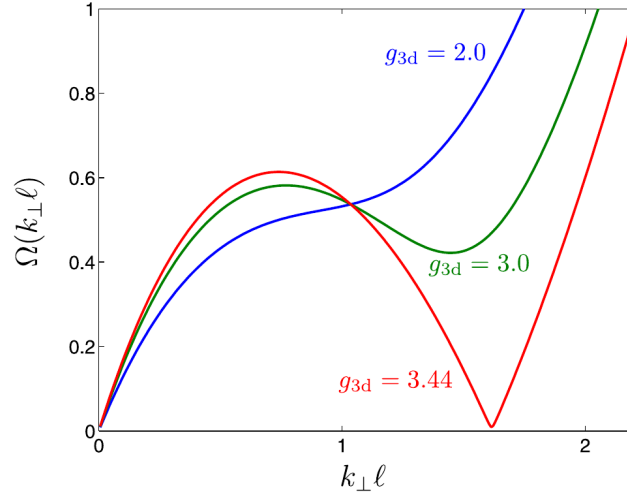


Figure 1.6. Excitation spectrum as a function of k_{\perp} ($\theta_k = \pi/2$) for different interaction strengths $g_{3D} = mD^2n\ell / (4\pi\hbar^2)$ calculated in [30]

the very interaction strengths. In Fig. 1.6 we see how the the excitation spectrum changes for different values of interactions strengths. Indeed, both k_{rot} and the roton energy can tuned in experiments by changing the trapping potentials, the system density or the interactions [30]. Keeping the first two fixed, when ϵ_{dd} reaches a critical value the roton energy touches the zero point and we encounter an instability where density perturbations with k_{rot} lead the system to the collapse. In this case the repulsive contact interactions are perfectly balanced by the mainly attractive part of DDI and a density perturbation with k_{rot} is energetically favored. This modulation can grow indefinitely in amplitude until three body losses, enhanced by the high densities in the peaks, become dominant and destroy the system.

The role of quantum fluctuations

This collapse can be avoided providing a stabilization mechanism that allows finite lifetimes for the density modulated superfluid. At the mean field level, we saw that the roton instability comes from the perfect balancing between contact and dipolar interactions which gives a vanishing energy cost for the density perturbations at k_{rot} . Including the DDI, the mean field interaction energy E_{MF} is given by [30]

$$E_{MF} = \frac{gn^2V}{2} (1 - \epsilon_{ddf}(\kappa)) \quad (1.15)$$

where f is a function of the aspect ratio κ of the condensate, accounting for the magnetostriction effect [44]. At the instability, $E_{MF} + E_{kin} \approx 0$ and we need to go to the second order, considering the quantum fluctuations. In non dipolar BECs, quantum fluctuantions are responsible for the depletion of the condensate (which is neglected at the mean field approach) that gives a correction to the energy of the ground state called Lee-Huang-Yang (LHY) term. This correction is given by

$$E_{LHY} = gn^2V \left[\frac{64}{15\pi} (na^3)^{\frac{1}{2}} \right] \quad (1.16)$$

which is proportional to $n^{5/2}$. The beyond mean field correction in the dipolar case, which has been calculated in [31], reads

$$E_{QF} = gn^2V \left[\frac{64}{15\pi} (na^3)^{\frac{1}{2}} \right] Q_5(\epsilon_{dd}) \quad (1.17)$$

where Q_5 accounts for the dipolar interaction, and is defined as

$$Q_5(\epsilon_{dd}) = \frac{1}{2} \int d\theta_k \sin \theta_k \left(1 + \epsilon_{dd} (3 \cos^2 \theta_k - 1) \right)^{\frac{5}{2}} \sim 1 + \frac{3\epsilon_{dd}^2}{2}. \quad (1.18)$$

The surprising result is that E_{QF} is isotropic, since Q_5 depends only on the value of ϵ_{dd} , and always ≥ 0 . This gives rise to a repulsive interaction, that can dominate near the roton minimum, where the mean field energy is extremely small. Furthermore, we can see that E_{QF} has the same dependence on density, $\propto n^{5/2}$, of the the LHY correction, while E_{MF} only depends quadratically on n . In terms of energy per particle this means that $E_{MF} \propto n \propto r^{-3}$, while $E_{QF} \propto n^{3/2} \propto r^{-9/2}$. This different dependence on the coordinates, can eventually lead to a local minimum in the total energy, hence to a metastable system [31].

The idea of stabilizing roton modes using quantum fluctuations have recently pushed many experiments to discover novel states of matter emerging from the interplay of long-range DDI and repulsive contact interactions. In particular, when the roton energy gap is positive we have a standard dipolar BEC, that is a superfluid phase. A cartoon view of such system is sketched in Fig. 1.7 (left), where we see a long wavelength modulation corresponding to phonon excitations. On the other hand, tuning ϵ_{dd} we can reach the extreme case of negative roton gaps (i.e. imaginary excitation energies): here the dipoles in the system forms an array of self bound droplets stabilized by the quantum fluctuations, called *droplet crystal*. As sketched in Fig. 1.7 (right), the density between the droplets is zero therefore there is no global coherence in the system. However, in the intermediate case (central panel) the density of the superfluid is periodically modulated, but does not vanish between adjacent sites: this allows atoms to be delocalized in the system, maintaining its global coherence. This counter-intuitive phase that mix together properties of superfluids (phase coherence) with those of solids (periodic density) realizes a so-called *supersolid*, and has been recently observed experimentally [45] with dipolar quantum gases. In Fig. 1.8 we see how, changing ϵ_{dd} we can pass from a standard BEC (upper panel) to an incoherent droplet crystal (bottom panel), crossing the supersolid phase transitions (central panel). In Fig. 1.9 we see that, at this transition, the Goldstone

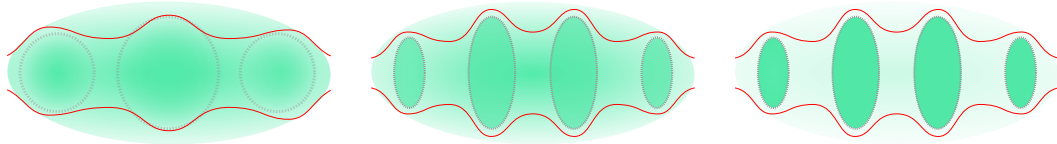


Figure 1.7. Cartoon view of an excited dipolar BEC (left), a cluster supersolid (center) and a droplet crystal (right). Red lines corresponds to the envelope of the density modulation. The color gradient corresponds to the system density.

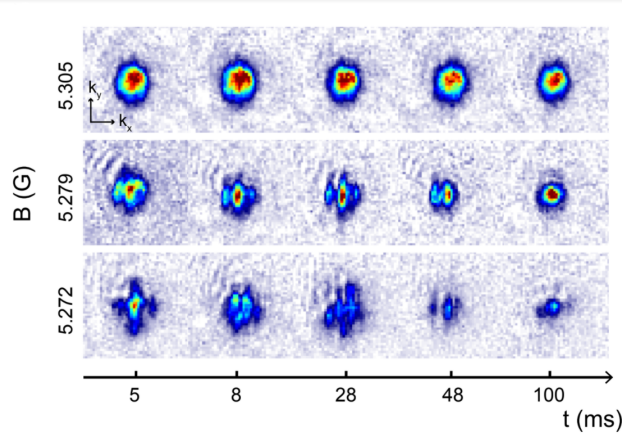


Figure 1.8. Momentum distributions of a dipolar quantum gas of ^{162}Dy as a function of the expansion time t for different values of magnetic field [45]. Different panels, corresponding to different scattering lengths a_s , show a typical BEC (upper panel), a supersolid phase (central panel) and an incoherent droplet crystal (lower panel).

mode associated to the broken gauge symmetry in the BEC side ($\epsilon_{dd} < 1.35$) splits into two. The lower energy mode is again associated to the superfluid and disappears in the droplet crystal phase. The high energy mode is instead associated to the spontaneous symmetry breaking of the translational symmetry, which marks the onset of supersolidity.

1.2 Strongly Dipolar Gases

In the previous sections we saw how new phenomena arising in dipolar quantum gases require, as a main ingredient, that DDI dominates in the system. Being the interaction energy proportional to D^2 , the straightforward approach is therefore to look for dipolar systems with dipole moments as large as possible, in order to naturally have $\epsilon_{dd} > 1$. The strongly interacting regime is reached when the dipolar scattering length is comparable with the inter-particle distance

$$a_{dd} \geq n^{-\frac{1}{\mathcal{D}}} \quad (1.19)$$

where \mathcal{D} is the dimensionality of our system.

Thanks to efficient and stable cooling and trapping methods, ultracold magnetic atoms like Cr [5], Er [1] and Dy [32] have been proven a reliable platform to study the physics of dipolar gases, but still with limited dipole moments, hence dipolar lengths, given the typical maximum densities that correspond to a length scale of about 100 nm. Much stronger dipole moments could be reached in principle in electric system, because electric dipoles are naturally larger than magnetic ones. Indeed, systems like Rydberg atoms or polar molecules exhibits electric dipole moments that correspond to dipolar lengths typically a few orders-of-magnitude larger than their magnetic counterparts. In Rydberg atoms, where a single electron is excited to s orbitals with high n (typically $n > 100$), one can easily obtain $\epsilon_{dd} \sim 10^3$ but at

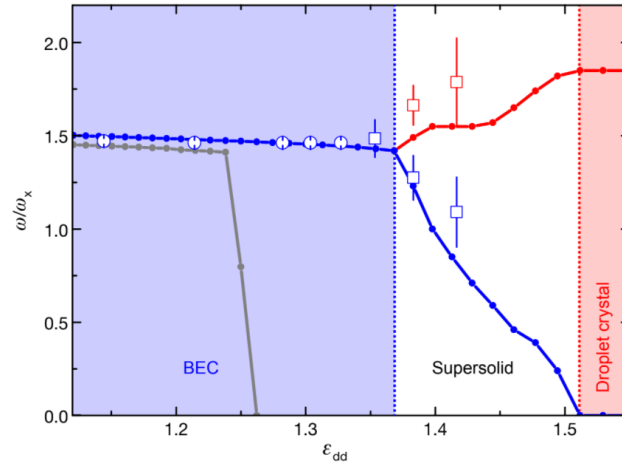


Figure 1.9. Breathing mode frequency as a function of ϵ_{dd} [47]. Solid lines are numerical simulations of GPE with (blue and red) and without the LHY term. The mode splitting after a critical value of ϵ_{dd} shows how two symmetries are broken in the supersolid phase.

the cost of very short lifetimes. Preventing the thermalization of the system, such strong dipolar interactions make the study of many-body physics at the equilibrium impossible. From this perspective, electric polar molecules are more promising, since they have large electric dipole moments and longer lifetimes. Nevertheless, the laser cooling and trapping of molecules have proven a real experimental struggle and a molecular degenerate gas starting from preformed molecules has not yet been achieved. This regime has been instead explored by associating molecules starting from a mixture of two atomic quantum gases. This method circumvents the cooling and trapping issues always present when working with molecules, and has been exploited recently to create a degenerate gas of fermionic polar molecules of $^{40}\text{K}^{87}\text{Rb}$ with $\epsilon_{dd} \sim 20$ [51]. These heteronuclear molecules are created in highly excited vibrational states, where atoms are weakly bound and the electric dipole moment is quenched. Therefore, in order to exhibit their strong dipolar nature, electric molecules have to be transferred to their ground state using techniques like stimulated raman adiabatic passage [18]. These procedures are extremely delicate and represent the main challenge in current experiments on ultracold molecules.

A new approach to the problem of achieving strongly dipolar systems consists in associating magnetic atoms in order to obtain homonuclear weakly bound molecules with large magnetic dipole moments. Differently from their electric counterpart, the dipole moment of magnetic molecules is not quenched in high vibrational states, since it depends only on how the atomic spins are coupled in the molecular state. In the optimal case, molecules have twice the magnetic moment of single atoms. Having also twice their mass, we can see from Eq. 1.6 that the molecular dipolar length is about 8 times the atomic one. This means that dipolar interaction energies are comparable with ones in the electric polar molecules case. The production of weakly bound magnetic molecules with large dipolar interaction has been demonstrated with erbium atoms in [17] starting from a cold sample of ^{168}Er in a quasi-two-dimensional harmonic trap. In the next sections I will focus on this production mechanism,

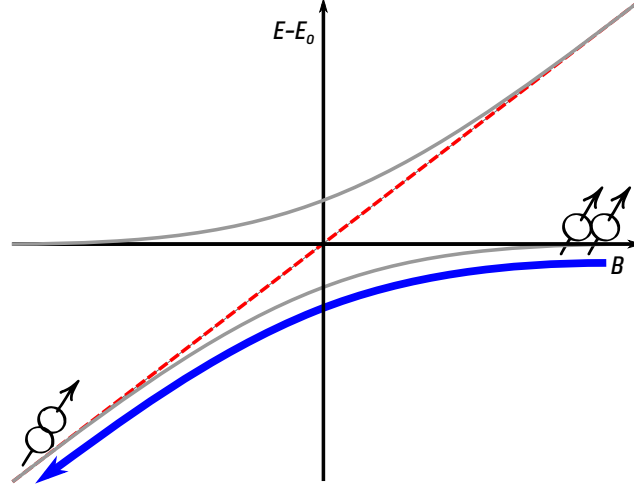


Figure 1.10. A cartoon view of the energy states involved in a Feshbach resonance, as a function of the external magnetic field. The open channel lies on the horizontal axis, while the bound state in closed channel is represented with dashed red line. The blue arrow, connect this two asymptotic states, representing the mechanism of molecules association by sweeping adiabatically the magnetic field across the resonance.

discussing the stability of these molecular gases in experiments.

Association of magnetic molecules

In section 1.1 we saw how Feshbach resonances can be exploited to tune contact interactions in ultracold quantum gases using a singularity in the scattering length caused by the crossing of two (or more) two-body states of the system. The very same phenomenon can be used to convert two colliding atoms in a weakly bound molecule. In the simple picture of a two-channel resonance, sketched in Fig. 1.4 (left), we considered a scattering state of the system (open channel) and a bound state in a higher energy molecular potential (closed channel). We already said that, these states have in general a different magnetic dipole moment μ , and therefore experience a non zero relative Zeeman shift $\Delta E = (\mu_1 - \mu_2) B$ in the presence of an external magnetic field. To understand the Feshbach association process we can look at Fig. 1.10, where the red dotted line corresponds to the energy of the bound state in the closed channel, relative to the scattering state energy $E_O(B)$ (lying on the x-axis). When we consider the coupling between open and closed channel, the new eigenstates of the system are the two gray branches depicted in Fig. 1.10. Far from the resonance these *dressed* states asymptotically tend to the old ones, while at B_0 they present an anti-crossing. The association mechanism consists in finely control the magnetic field, sweeping it across the resonance, in order to walk the system down the lower branch [11].

Obviously, this mechanism can be used for molecular association only when suitable Feshbach resonances are available at magnetic fields reasonably low. This is not a problem with dipolar atoms, since they have a very dense and broad spectrum of resonances [34, 40]. Nevertheless, to choose the right one we have to consider

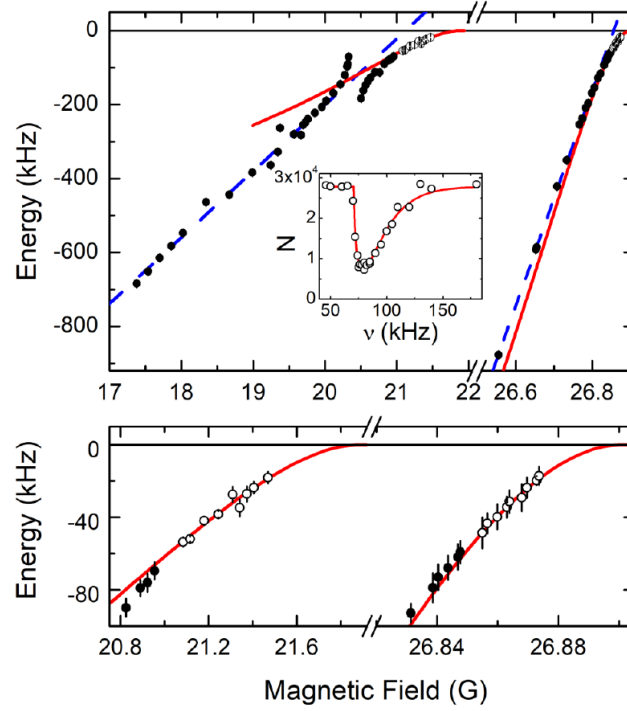


Figure 1.11. Binding energy of two bound states in ^{162}Dy measured in [33]. These states correspond to two Feshbach resonances respectively at $B_{01} = 21.9$ G and $B_{02} = 26.9$ G. The width of the two resonances are $\Delta_{01} = 1.97$ G and $\Delta_{02} = 0.14$ G.

two main aspects. In general broad resonances corresponds to weakly bound states with higher magnetic dipole moments. This can be intuitively understood looking once again at Fig. 1.10. The maximum μ is achieved when the bound state has the same magnetic moment of the two atoms in the open channel, hence when the red dashed line lies on the horizontal axis. When μ decreases, the red line is steeper and the resonance narrower. Broad resonance are therefore desirable for the realization of strongly dipolar gases, as we want for our system the largest magnetic dipole moment. However, considering the dense Feshbach spectrum of dipolar atoms, it is common for one or more very sharp resonances to be found across broader ones. This could lead to non-adiabatic effects causing losses. Indeed, to efficiently convert atoms into molecules, we must cross the resonance adiabatically, i.e. the system must stay in the same quantum state (the lower branch) during the magnetic field sweep.

A couple of broad Feshbach resonances of ^{162}Dy have been studied in [33], together with the binding energies of the molecular states reported in Fig. 1.11. Here, the resonance at lower field has a width of about $\Delta \sim 2$ G and about twice the magnetic moment of single dysprosium atoms.

Another important aspect that has to be taken into account, concerns the association efficiencies. These are typically quite low (less than 10%) in the case of thermal gases, as the one reported in [17], since thermal excitations of the system can lead to non-adiabatic processes that cause atoms to return in their scattering state, or

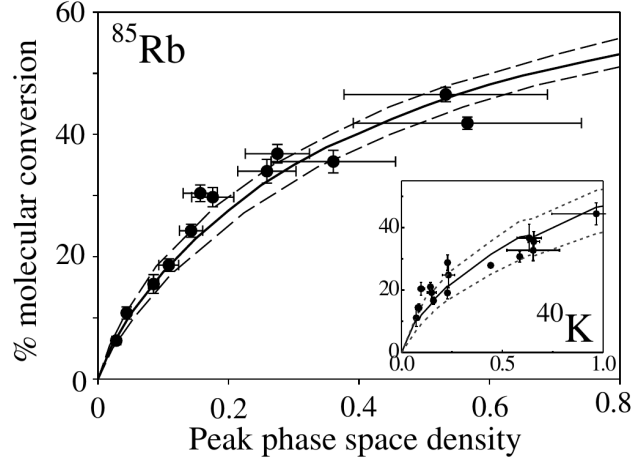


Figure 1.12. Molecule conversion efficiency in alkali atoms as a function of phase space density [23]. Solid lines are numerical simulation, while dashed lines corresponds to the uncertainties in the numerical model.

worse, being lost due to inelastic collisions. Differently, the molecular production efficiency is expected to be much higher in the degenerate regime. Indeed, as one can see in Fig. 1.12, the efficiency tends to 1 when phase-space density approaches 1. This has been demonstrated with alkali atoms in [23] where authors compare the experimental results obtained for rubidium, with the theoretical model presented in [20]. However, thinking about unitary efficiencies is unphysical and pure molecular gases cannot be obtained by Feshbach association. The experimental strategy that can be used to produce such systems, is therefore to go for the highest possible efficiency and then remove the remaining unbound atoms in the sample. This can be done by simply shining a pulse of light that is resonant with an atomic optical transition, but not with any molecular transition.

Molecules stability

Molecules produced with this method have energies of the same order of E_O , therefore they are in the highest vibrational state. As a natural consequence, their lifetime is strongly limited by decay processes towards the ground states, lying hundreds of THz in energy below the atomic threshold. These processes are mainly caused by three-body inelastic collisions at short range, enhanced by the attractive part of the dipolar interaction. In three-dimensional dipolar systems the rate of inelastic collisions $\Gamma_{inelastic}$ scales as the square of the dipole moment, as it does the interaction strength. This fact represents a real *bottle-neck* for the experimental exploration of strongly dipolar systems, where lifetimes are drastically reduced by such collisions. The only way to prevent this dramatic effects is to realized two-dimensional systems, where, as we will see in this section, collision rates are strongly reduced.

Remarkably, as we can see in Fig. 1.13 (left), the rates of inelastic collisions in dipolar systems show a universal behavior that has been investigated in [26, 41, 49]

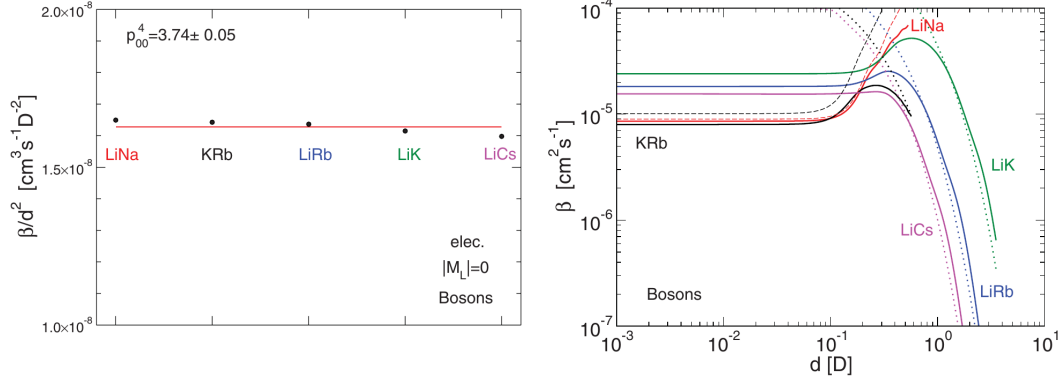


Figure 1.13. Loss rates for bosonic electric molecules calculated in [41] in three-dimensions (left) and in a two-dimensional system (right). The left plot shows how, in the van der Waals regime, β depends only on the square of the dipole moment d , with a characteristic coefficient 3.74 (see Eq. 1.21). The right plot, shows the suppression of β when a_{dd} becomes larger than the harmonic oscillator length. Here, dashed and dotted curves correspond respectively to the quasi-2D model in Eq. 1.22 and to the 2D model in Eq. 1.23.

in the case of electric polar molecules. Losses due to inelastic collisions are described by the following differential equation

$$\frac{\partial n}{\partial t} = -\beta n^2 \quad (1.20)$$

where $\Gamma_{inelastic} = \beta n$ is the collision rate of the system. In three dimensions β can be studied using a *Quantum Threshold* model that takes into account van der Waals and dipolar interactions, assuming a full loss when molecules come near each other [41]. This latter circumstance happens with a probability that depends on the interaction potentials among molecules, therefore β depends both on the van der Waals and dipolar interactions, accordingly to

$$\beta^{3D} = 2\pi \left[1.92 \left(\frac{2\hbar^2 C_6}{m^3} \right)^{\frac{1}{4}} + 3.74 \left(\frac{\sqrt{16/30}}{\hbar} \right) \left(\frac{D^2}{4\pi} \right) \right]. \quad (1.21)$$

The first term in the latter equation takes into account the $1/R^6$ dependence of the van der Waals interaction in Eq. 1.4, which we expect to be small with respect to the second term, corresponding to the dipolar part. The numerical coefficients weighing the two terms, result from the numerical simulation carried out in [41].

When we observe the dynamics of dipolar molecules in two-dimensions we find a very different scenario. Indeed, looking at Fig. 1.13 (right), we clearly see that inelastic collisions are strongly suppressed in the dipolar regime, where β drops by orders-of-magnitude. This can be intuitively understood, thinking at the mechanics of dipolar interactions in two-dimensions. In particular, when dipoles are tightly confined along their polarization axis they cannot interact in head-to-tail configuration, and the attractive part of DDI is strongly inhibited [4]. The interactions among the dipoles are mainly repulsive, and the probability for three molecules to come closer to each

other drops. From this point of view the strength of the confinement, that can be quantified by the harmonic oscillator length ℓ_z along the polarization axis, plays an important role. When $\ell_z \gg a_{dd}$, we are in the so-called quasi-2D regime, in which collisions have still a 3D nature and the collisional rates given by the Quantum Threshold model are just rescaled by a geometric factor

$$\beta^{Q2D} = \sqrt{\frac{m\omega_z}{4\pi\hbar}} \beta^{3D}. \quad (1.22)$$

As we can see from Fig. 1.13 (right), in this regime β^{Q2D} is of the same order of β^{3D} , since the attractive part of DDI is only slightly reduced. On the other hand, when $\ell_z \ll a_{dd}$, interactions are effectively in 2D, where our intuitive explanations of the inelastic collisions suppression holds. In this case β is given by

$$\beta^{2D} = 2 \frac{13\hbar}{m} \left(\frac{2E_c}{\hbar\omega_z} \right)^2 \exp \left[-2 \left(\frac{a_{dd}}{\ell_z} \right)^{\frac{2}{5}} \right] \quad (1.23)$$

where the exponent $2/5$ inside the exponential has been determined by the numerical simulations carried out in [41]. Here the threshold energy E_c does not depend on the interactions, but it is fixed by the temperature of the two-dimensional gas. Note that, even if the 2D model should hold only for dipolar lengths much longer than ℓ_z , in real systems Eq. 1.23 gives correct predictions starting from dipolar lengths of the same order of ℓ_z [41].

1.3 Superfluidity in two dimensions

In this section, I will present the basics of Bose-Einstein condensation for a trapped gas in lower dimensions and discuss new effects arising especially in 2D, when we take interactions into account.

Superfluidity in three spatial dimensions is directly linked to the condensation of bosons that, populating macroscopically their ground state, break the gauge symmetry of the system giving rise to a single wave function with global phase. In this picture, superfluidity reflects the long range order linked to this spontaneous symmetry breaking. This is not the case for a two-dimensional infinite system, where the BEC transition cannot happen at non-zero temperatures, thus preventing the emergence of a true long range order within the system [22]. Nevertheless, an interacting Bose gas in 2D could still become a superfluid at $T \neq 0$ [6], thanks to the existence of a quasi long-range order due to the suppression of thermal fluctuations. The transition to the normal state has a different nature from the BEC transition, and has been studied theoretically by Berezinskii-Kosterlitz-Thouless (BKT) [28]. The overall picture for the superfluid state in 2D is that of a quasi-ordered state in which phase fluctuations are strongly suppressed and correlations decay slowly with the distance [22]. At this low temperature state, vortices and anti-vortices, which are responsible for phase fluctuations, are bound together in pairs providing a topological order that suffices for superfluidity. Instead, above a certain critical temperature the pairs uncouple, destroying the coherence in the system.

In trapped gases this scenario is even richer. Indeed, the density of states of the free case is modified by the finite size of the system, enabling the possibility to have both BEC and BKT transitions, occurring at different temperatures, depending on the density and the strength of the interactions. When we consider repulsive contact interactions, the critical temperature for BEC typically drops as the density at the trap center decreases due to repulsion between the particles. On the contrary, the BKT critical temperature increase for increasing interaction strengths. So, when the temperature decreases at fixed interactions, the system crosses the BKT transition first and then the BEC transition. In this process, known as *BKT-driven condensation* [22], the emergence of a condensed fraction right after the transition is once again caused by the finite size of the system. Indeed, in the quasi-ordered state correlations decay slow enough to have coherence lengths comparable with the system size: in this sense the gauge symmetry is locally broken and BEC occurs.

Condensation in 2D

For an ideal three-dimensional Bose gas, the normal-to-superfluid transition occurs when the particle thermal wavelength $\lambda(T)$ approaches the interparticle distance, or equivalently when the phase-space density $n\lambda^3(T) \sim 1$. Keeping T fixed, the population of the excited states N_{exc} saturates, at this point, to a critical value N_c leading to a macroscopic occupation of the ground state for an increasing particle number N . This is the well known phenomenon of Bose-Einstein Condensation. From an experimental point of view, it is common to fix N and define a critical temperature T_{BEC} below that an ultracold bosonic gas undergo this phase transition and becomes superfluid.

Considering a non-interacting system at the continuum limit, i.e. $\delta\varepsilon \ll k_B T$ with $\delta\varepsilon$ being the spacing of energy levels of the system, N_{exc} is given by

$$N_{exc} = \int_0^{+\infty} \rho(\varepsilon) \frac{z}{e^{\beta\varepsilon} - z} d\varepsilon \quad (1.24)$$

where $\rho(\varepsilon)$ is the density of states, $z = e^{\beta\mu}$ is the fugacity of the system and $\beta = 1/k_B T$. In order to get $T_{BEC} \neq 0$, the limit of Eq. 1.24 for $z \rightarrow 1$ needs to be a finite value N_c :

$$N_{exc} \xrightarrow{z \rightarrow 1} N_c < \infty . \quad (1.25)$$

In a two-dimensional infinite system, the density of states does not scale with the energy as in 3D, but is a constant, $\rho \sim \text{const.}$ This difference has a dramatic impact on Eq. 1.24, which has always a solution with $N_{exc} = N$ for $T > 0$, so BEC can exist only at $T = 0$. BEC can be restored in trapped gases, since the confining potential restores an energy-dependent density of states. For an harmonic confinement $V_{ho}(\mathbf{r}) = \frac{m}{2}\omega^2 \mathbf{r}^2$ the density of states changes with dimensionality as

$$\rho_{ho}^{(\mathcal{D})}(\varepsilon) = \frac{\varepsilon^{\mathcal{D}-1}}{(\hbar\omega)^{\mathcal{D}} (\mathcal{D}-1)!} . \quad (1.26)$$

If we now take $\mathcal{D} = 2$, we see that $\rho_{ho} \sim \varepsilon$ and the condition in Eq. 1.25 is satisfied, therefore we obtain a critical temperature for the transition

$$T_{BEC} = \frac{\hbar\omega_r}{k_B} \frac{\sqrt{6N}}{\pi} \quad (1.27)$$

that is non zero in the thermodynamic limit ($N \rightarrow \infty$, $\omega_r \rightarrow 0$, $N\omega_r^2 = \text{const}$) [22]. This case corresponds to a confinement potential V_{ho} with trap frequencies $\omega_x = \omega_y = \omega_r$ and $\omega_z \gg \omega$, that well describes optical trapping potentials generally used in experiments. Note that the ideal 2D system would require an infinitely large ω_z , but as long as $\hbar\omega_z \ll k_B T$ we have a *thermodynamical 2D* system and Eq. 1.27 holds.

Another more intuitive way to think to the BEC transition in lower dimensions involves thermal excitations of the system. In particular, large wavelength phonons in 2D have a diverging infrared contribution, due to the fact that the density of states does not go to zero for vanishing energy, so they are able to destroy the long range order underlying superfluidity: the only chance to have a condensate exists at $T = 0$, where no phonons are present. These diverging modes are excluded in a trap by the finite size of the system that sets a cutoff on phonons maximum wavelength.

Interactions in 2D

When interactions in the gas are taken into account, Eq. 1.27 is not valid, and a mean field analysis is required. Nevertheless, for weak interactions corrections are expected to be small enough for T_{BEC} to good estimate the actual critical temperature for BEC transition [39].

On the other hand, interaction are crucial for the emergence of the quasi-ordered state in the BKT transition. At this level I will only take contact interactions into account, adapting the parameters introduced in section 1.1 to the case of thermodynamical 2D system in a harmonic trap (as the one described in the previous section). When the harmonic oscillator length ℓ_z is shorter than the interaction range, which is the scattering length a_s , interactions effectively happen in two-dimensions and the system is in the *collisional 2D* regime. In the opposite limit, i.e. $\ell_z \gg a_s$, interactions are still in 3D and the coupling constant g can be simply rescaled to give an interaction energy

$$E_{int} = \frac{g}{2} \int n_{2D}^2(\mathbf{r}) d^2r \quad (1.28)$$

where $g = \frac{\hbar^2}{m} \tilde{g}$ proportional to the dimensionless parameter quantifying the interaction strength

$$\tilde{g} = \sqrt{8\pi} \left(\frac{a_s}{\ell_z} \right). \quad (1.29)$$

From the last equation we see that, for fixed a_s , the weakly interacting regime corresponds to the thermodynamical 2D case, where $\tilde{g} \ll 1$. Furthermore, it is interesting, from the experimental point of view, that changing the confinement

along z directly affects the interaction strength within the system. The strongly interacting regime, i.e. when $E_{int} = E_{kin}$, is reached for $\tilde{g} \approx 2\pi$ [22].

Berezinskii-Kosterlitz-Thouless transition

Let us now focus on the BKT transition for weakly interacting gases in 2D. As we saw in previous sections, a non interacting gas in an infinite 2D system can be superfluid only at zero temperature due to the presence of thermal fluctuations that destroy the long range order at $T > 0$. This picture drastically changes in interacting gases.

The main effect of interactions with respect to the ideal Bose gas, involves the density fluctuations in the system. When the temperature is low enough, so that $n\lambda(T) \gg 1$, density fluctuations on large scales (compared to the healing length of the system) are strongly suppressed: the remaining perturbations with small wavelength do not diverge in 2D and cannot destroy superfluidity [22]. Differently, phase fluctuations at large scales (phonons) are not suppressed because they have a vanishing energy cost for $k \rightarrow 0$.

In the BKT theory, phonons are not the only relevant excitations and one has to consider also *vortices*. These are zero density points around which the superfluid has a quantized circulation κ that gives an irrotational velocity field

$$v_s(r) = \frac{\kappa}{2\pi r} \quad (1.30)$$

with r being the distance from the vortex center. These excitations can be thought as quasi-particles with quantized angular momentum being an integer multiple of \hbar . Like any other particle has a corresponding anti-particle, vortices have anti-vortices which have negative angular momentum since they have a circulation with opposite sign. Below the critical BKT temperature vortices and anti-vortices are excited in bound pairs, keeping the total angular momentum of the system constant. The pairs contribute only to phase fluctuations with short wavelengths and provide a topological order emerging in the system. On the other hand, this is destroyed above the critical temperature by the pair unbinding and proliferation of free vortices and anti-vortices.

The topological order given by this mechanism cannot be altered by the phonons, which contribute only with smooth variations of the phase, and is sufficient for superfluidity. We therefore identify the critical temperature for the BKT transition as the point at which this topological order is destroyed. A general result of the BKT theory is that this corresponds to a critical phase space density [22]

$$n \lambda(T_{BKT}) = \ln \left(\frac{C}{\tilde{g}} \right) \quad (1.31)$$

where $C = 380 \pm 3$ is a constant that can be extracted from numerical Monte-Carlo simulations. This defines a critical temperature

$$T_{BKT} = \left(\frac{\hbar^2}{2\pi m k_B} \right) \frac{n}{\ln(C/\tilde{g})} . \quad (1.32)$$

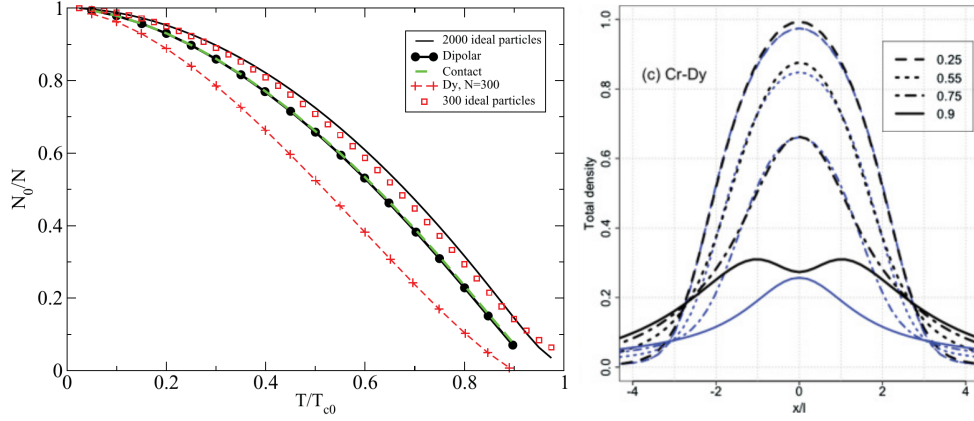


Figure 1.14. Condensed fraction as a function of the temperature in dipolar gases (left) and density profile of dipolar condensates (right). In the left plot, solid black line is the ideal case of $N = 2000$ non interacting particles; the dipolar (chromium) and contact gases with $N = 2000$ corresponds respectively to the black line with dots and the green line. Red squares and crosses corresponds respectively to $N = 300$ ideal particles and $N = 300$ dipolar (dysprosium) atoms. In the right plot, blue curves corresponds to chromium, while black ones represents dysprosium. [50]

that holds for infinite systems with constant density.

What happens with DDI?

So far we have discussed the phenomenon of superfluidity in two-dimensional systems, considering two extreme cases. On one side we have non interacting trapped gases, in which BEC transition happens at T_{BEC} given by Eq.1.27. On the other we saw weakly interacting gases in infinite systems, where the BKT transition temperature follows Eq.1.32. In the case of dipolar quantum gases, we expect that this latter case will be modified from both the finite size of the system and the presence of DDI. As we saw in Section 1.1 these are long range, anisotropic interactions which are attractive when two dipoles are in head-to-tail configuration, and repulsive when they are sitting side-by-side.

The effects of dipolar interaction on the BKT critical temperature have been investigated theoretically in [16, 50]. In Fig. 1.14 (left) we can see the results of the numerical simulation carried out in [50] for the condensed fraction as a function of the temperature. Here we see that, with respect to non dipolar gases, the critical temperature changes only slightly and the condensed fraction at a given temperature changes at most by about 15%. This variations can be explained by observing the density profile of the trapped gas below the critical temperature, reported in Fig. 1.14 (right). Indeed, the repulsive part of DDI produces a strong depletion of the condensate, therefore a lower density at the trap center.

Intuitively, the effect of the interactions is less important for larger systems. In particular, this has been pointed out in [16], where the behavior of T_{BKT} in dipolar gases has been investigated changing the system size. The result of the numerical

simulations shows that

$$T_{BKT}(L) = T_{BKT}(\infty) + \frac{b}{\ln^2(L)} \quad (1.33)$$

where b is a constant and $L = \sqrt{N}$, with N being the total number of particles. This results shows how the critical temperature decreases for increasing L .

Chapter 2

Design of a two dimensional system

In this Chapter I will discuss how the idea of realizing a strongly dipolar superfluid in two dimensions can be implemented starting from the experimental set-up operating at the Dysprosium Laboratory of CNR-INO and LENS, in Pisa. The various theoretical concepts I presented separately in Chapter 1, here are combined together and translated into the experimental language. This will also require the introduction of some additional technical concepts, related to the cooling and trapping methods used in our experiment, that are the object of the first two sections of this Chapter.

2.1 Experimenting with dysprosium

As I briefly mentioned at the end of Section 1.1, our experiment is based on a dipolar Bose-Einstein condensate of dysprosium. In its ground state the electronic configuration is $[\text{Xe}]^{10} 6s^2$, leading to a state $^5\text{I}_8$ with a total angular momentum $J = 8$. Bosonic isotopes of dysprosium, as ^{162}Dy used in our experiment, have zero nuclear spin, hence do not have hyperfine structure. The level structure is sketched in Fig. 2.1, where the two cooling transitions used in the experiment are highlighted.

The dysprosium machine used in our experiments is reported in Fig. 2.2. Dysprosium melts at $T = 1412^\circ\text{C}$, therefore, to obtain a thermal gas we heat a dispenser filled with solid dysprosium at $T \sim 1200^\circ\text{C}$ inside an oven, where the vapor tension is high enough to produce a hot atomic beam. Atoms in this beam needs to be slowed down in order to be captured by the magneto-optical trap (MOT) where the first cooling step is performed. This is done with a Zeeman slower working with blue light at 421 nm. This device exploits the radiation pressure force exerted by resonant photons on the incoming atoms to slow them down from an initial speed of about 500 m/s to something around 10 m/s, using a custom magnetic field gradient to compensate the atomic Doppler shift during the motion. The blue transition has a broad natural linewidth of 32.3 MHz and is used also for the imaging system and the transverse cooling. The latter helps to reduce the divergence of the hot atomic beam at the oven exit. The slowed atoms are then loaded in the MOT, situated in the main cell under ultra high vacuum ($P < 10^{-10}$ mbar). Here the light

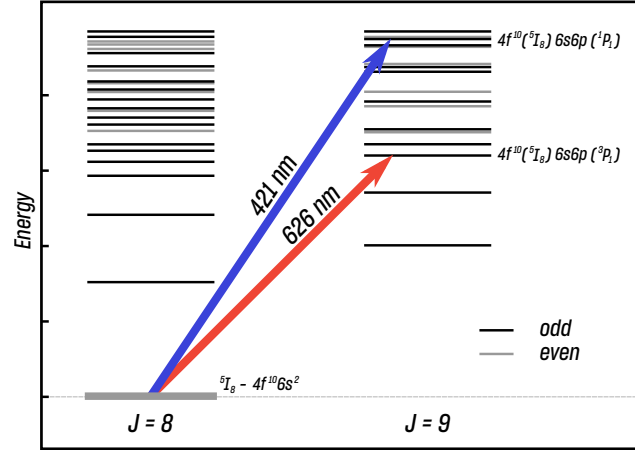


Figure 2.1. Level structure of dysprosium together with the cooling transitions used in the experiment.

at 626 nm is used in combination with a quadrupole magnetic field, to provide at the same time cooling and confinement for the atoms. The lower bound in MOT temperature is set by the minimum Doppler temperature which is proportional to the natural width of the transition used, which is 136 kHz for the 626 nm transition. This is the reason why we use red light, that having a much narrower width than blue one, allow much lower temperatures of about 3.3 μK , despite of lower capture velocities. The typical densities and temperatures of the system in the MOT are about 10^{11} cm^{-3} with $T \sim 20 \mu\text{K}$. At this point, dysprosium atoms are still hot with respect to the temperature scales of Bose-Einstein condensation, and need to be transferred in purely optical traps for the evaporative cooling that brings the system to quantum degeneracy. At the end of this cycle we end up with a BEC of about 40000 dysprosium atoms with a temperature around 10 nK. The critical temperature for the condensation is 60 nK.

On the right panel of Fig. 2.2 we can see the scheme of the optical traps used in the evaporation process. The final trap that holds the BEC during measurements has the shape of an ellipsoid, with trap frequencies of $\nu_x = 20 \text{ Hz}$, $\nu_y = 50 \text{ Hz}$ and $\nu_z = 80 \text{ Hz}$ along the three spatial dimensions. This elongated shape prevents the collapse of the system due to magnetostriction [44], limiting the attractive part of dipolar interaction.

In the next section I will focus on the basic theory of optical dipole traps, summarizing the key aspects that we need to keep in mind for the design of the new experiment.

2.2 Optical Dipole Traps and Lattices

Optical dipole traps are conservative traps that use the Stark shift of atomic levels, induced by a laser electric field, as an effective potential able to confine the atomic motion. In the simple picture of an atom with only two levels separated by an energy

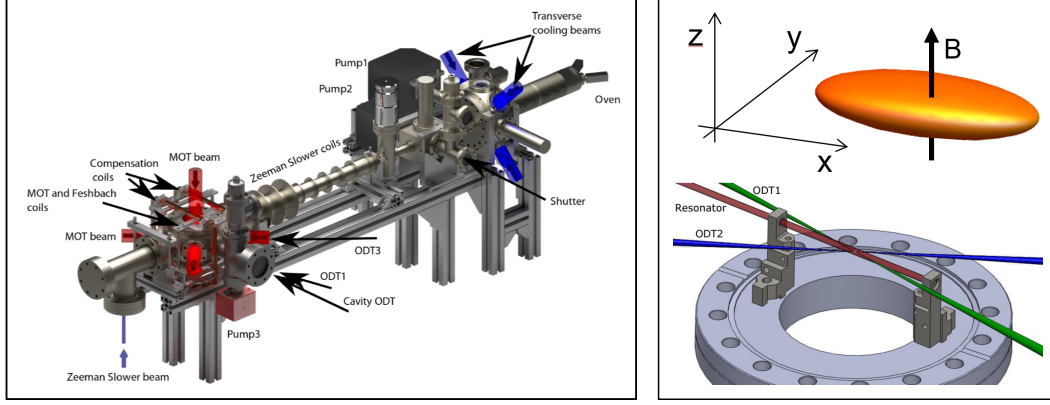


Figure 2.2. The dysprosium machine (left) and a detail showing the optical dipole traps used in our experiment (right).

$\hbar\omega_0$, the Stark shift for a non-resonant laser field is given by

$$\Delta \approx \frac{\Omega_{eg}^2}{4\delta} \quad (2.1)$$

where $\Omega_{eg} = \mathbf{d}_{eg} \cdot \mathbf{E}/\hbar$ is the Rabi frequency for the $g \leftrightarrow e$ transition and $\delta = \omega - \omega_0$ is the laser detuning [13]. Since $\Omega_{eg} \propto E$, the Stark shift is proportional to the laser intensity profile, that is well described by Eq. A.13 in the case of a focused laser beam. In particular for red-detuned light ($\delta < 0$) the Stark shift is negative and has a minimum at the intensity peak. Atoms moving away from this minimum experience an increasing effective potential, that can be well described as an harmonic well potential [21]

$$U_{dip}(r, z) = -U_0 + \frac{1}{2}m(\omega_r^2 r^2 + \omega_z^2 z^2) \quad (2.2)$$

where U_0 is the trap depth and $\omega_{r,z}$ are the trap frequencies given by

$$\omega_r^2 = \frac{4U_0}{mw_0^2}; \quad \omega_z^2 = \frac{2U_0}{mz_R^2}. \quad (2.3)$$

This trapping mechanism, pioneered by the Nobel laureate A. Ashkin [3], quickly leaked out of the field of atomic physics finding many fundamental application in biology, where the so-called *optical tweezers* (single focused beams) are used to trap particles up to 10 μm in size. In this case, as well as in the case of multi-level atoms like Dy, it is more convenient to think at the energy shift Δ as the polarization energy of the particle in the non-resonant field with amplitude \mathcal{E}

$$U = -\frac{1}{4}\alpha(\omega)\mathbf{E}^2. \quad (2.4)$$

Here α is the dynamical polarizability of the particle that, assuming a linear response, expresses the proportionality between the mean induced dipole moment and the oscillating field: $\langle \mathbf{d}(t) \rangle_t = \alpha(\omega)\mathcal{E} \cos \omega t$. Very far from resonances, the polarizability α takes a constant value and the energy in Eq. 2.4 takes the form of the effective potential in Eq. 2.2, with trap depth

$$U_0 = \frac{\alpha I_0}{2\epsilon_0 c} \quad (2.5)$$

where $I_0 = 2P/\pi w_0^2$ is the peak intensity of the laser beam.

The use of a single beam provides a trapped gas elongated on the beam propagation axis as shown in Fig.2.3 (left). To provide a three-dimensional optical confinement a second laser beam with different polarization (preventing interference effects) could be used to realize a so-called *crossed-beam* configuration Fig.2.3 (right). Here the trap frequencies along \mathbf{x}, \mathbf{y} and \mathbf{z} directions defines the aspect ratio of the trap: in isotropic spherical traps we have $\omega_x = \omega_y = \omega_z$, but it is also possible to work in anisotropic traps by changing the beam relative inclinations and intensities. For example we have *cigar-shaped* geometries when $\omega_x = \omega_y = \omega_r$ and $\omega_r \gg \omega_z$, on the other hand when $\omega_z \gg \omega_r$ the trap resembles a disk or, as it is more commonly described, a *pancake*. Intuitively pushing the ratio ω_r/ω_z to extreme values we can reach *quasi-1D* or *quasi-2D* geometries respectively in the cigar and pancake cases.

When two coherent beams are superimposed the optical potential follows the interference pattern of light intensity, giving rise to a periodic effective potential called *optical lattice* [21]. Considering two counterpropagating beams with electric fields $\mathbf{E}_1, \mathbf{E}_2$ with equal amplitude \mathcal{E} and wavelength λ , the total electric field is given by

$$\mathbf{E} = 4\hat{\mathbf{e}}\mathcal{E} \cos(kz - \omega t) \quad (2.6)$$

Using Eq. 2.4 we obtain a lattice potential 4 times deeper than the single beam one, with periodicity $\lambda/2$ along the propagation direction of the beams \mathbf{z} given by the interference term proportional to $\cos^2(kz)$. Each lattice site is described by a potential with the same form of Eq. 2.2 with $U_0 \rightarrow U_\ell = 4U_0$, and trap frequencies given by [36]

$$\omega_r^2 = \frac{4U_\ell}{mw_0^2}; \quad \omega_z^2 = \frac{2U_\ell}{m(d_\ell/\pi)^2} \quad (2.7)$$

where d_ℓ is the lattice spacing. This can be tuned by changing the relative inclination of the beams θ and can be derived geometrically as

$$d_\ell = \frac{\lambda}{2 \sin(\theta/2)} \quad (2.8)$$

that reduces to $\lambda/2$ in the counterpropagating configuration ($\theta = \pi$). This is typically done using a mirror back reflecting the incoming beam which is then refocused on the atomic sample. Adding back-reflected beams along other spatial dimension allows build also 2D or 3D lattices. The 1D case is showed in Fig. 2.3 (center).

The lattice depth U_ℓ must be compared to the recoil energy E_{rec} associated to absorption of a photon with momentum $\hbar k = \hbar\pi/d_\ell$ from the lattice

$$E_{rec} = \frac{\hbar^2 \pi^2}{2md_\ell^2}. \quad (2.9)$$

In practice we use the dimensionless parameter $s = U_\ell/E_{rec}$ to conveniently measure the lattice depth and, eventually, the tunneling between adjacent sites. Indeed, the tunneling energy in units of E_{rec} given in [36] is

$$\frac{J}{E_{rec}} = \frac{4}{\sqrt{\pi}} s^{\frac{3}{4}} \exp(-2\sqrt{s}) \quad (2.10)$$

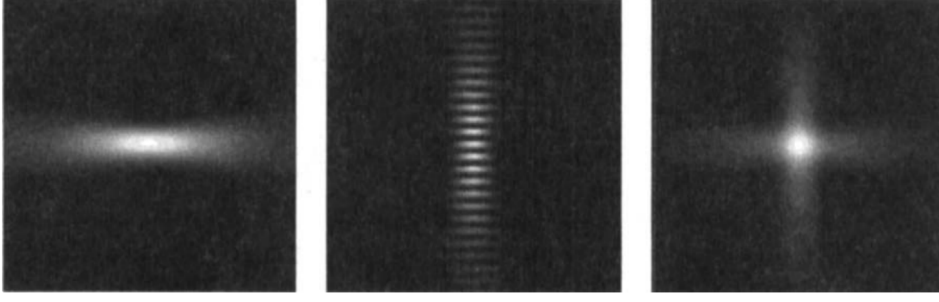


Figure 2.3. Light intensity profiles for different dipole traps calculated in [21]. From left to right: a single beam dipole trap, a one-dimensional optical lattice and crossed beam trap

and exponentially decay for growing s .

Heating rates in optical traps

Atoms trapped in optical lattices or dipole traps are dramatically sensible to the noise in both light intensity and beam position, which respectively produce fluctuations of the trap frequencies and trap dislocations. These noise sources provide an heating of the system leading to atom losses, hence to finite trapping times. The heating rates in far-detuned optical lattices can be studied using the time-dependent perturbation theory on the perturbed harmonic oscillator hamiltonian

$$\mathcal{H}_\gamma = \frac{\mathbf{p}^2}{2M} + \frac{1}{2}M\omega_{trap}^2 [1 + \gamma(t)] x^2 \quad (2.11)$$

where $\gamma(t) = (I(t) - I_0)/I_0$ are the intensity fluctuations. In the same way, the trap shaking can be taken into account considering fluctuations $\chi(t)$ of the atom position, hence the hamiltonian

$$\mathcal{H}_\chi = \frac{\mathbf{p}^2}{2M} + \frac{1}{2}M\omega_{trap}^2 [x - \chi(t)]^2 . \quad (2.12)$$

To obtain the heating rates we must first calculate the average transition rate between two harmonic oscillator energy states, $|n\rangle$ and $|m\rangle$, with the perturbation \mathcal{H}' in a time interval T , given by

$$R_{n \rightarrow m} = \frac{1}{T} \left| -\frac{i}{\hbar} \int_0^T dt' \mathcal{H}'_{n,m}(t') e^{i\omega_{mn}t'} \right|^2 . \quad (2.13)$$

The mean absorbed energy in the process is the heating rate, defined as

$$\langle \dot{E} \rangle = \sum_{n,m} P(n) \hbar \omega_{mn} R_{n \rightarrow m} \quad (2.14)$$

where we have to sum over all the $|m\rangle$ and $|n\rangle$ states, with $P(n)$ being the probability to populate the initial state. These calculations are carried out in [43] for both \mathcal{H}_γ and \mathcal{H}_χ . In the first case the heating rate is directly proportional to the average

system energy, $\langle \dot{E} \rangle = (\tau_\gamma)^{-1} \langle E \rangle$, leading to an exponentially increasing heating rate with time constant

$$\frac{\langle \dot{E} \rangle}{\langle E \rangle} = (\tau_\gamma)^{-1} = \pi^2 \nu_{trap}^2 S_\gamma (2\nu_{trap}) \quad (2.15)$$

where S_γ is the one-sided power spectrum of the light intensity noise. Considering the trap shaking, the heating rate does not depend on energy (i.e. it is constant in time), nevertheless it is possible to define a time scale dividing $\langle \dot{E} \rangle$ for the energy of the zero point motion of the trapped atoms, obtaining

$$\frac{\langle \dot{E} \rangle}{\langle E_0 \rangle} = (\tau_\chi)^{-1} = \pi^2 \nu_{trap}^2 \frac{S_\chi(\nu_{trap})}{\langle x^2 \rangle} \quad (2.16)$$

where $\langle x^2 \rangle$ is the mean squared position of a trapped atom and S_χ is the power spectrum associated to the fluctuations $\chi(t)$.

2.3 Designing the system

The idea behind this work resides in the possibility to use a one-dimensional optical lattice to obtain a 2D degenerate gas of Dy_2 weakly bound magnetic molecules, starting from the 3D Dy BEC described in section 2.1. The problem addressed in this section, constituting one of the results of this thesis, is to simulate this strongly dipolar superfluid, taking into account all the different physical phenomena explained in Chapter 1. From the theoretical aspects presented in Section 1.2, we understood that a superfluid made of strongly dipolar molecules can be stable only in two dimensions where inelastic collisions at short range are suppressed, and their rates scale as

$$\beta^{2D} = 2 \frac{13\hbar}{m} \left(\frac{2E_c}{\hbar\omega_z} \right)^2 \exp \left[-2 \left(\frac{a_{dd}}{\ell_z} \right)^{\frac{2}{5}} \right]. \quad (2.17)$$

Furthermore, in Section 1.3 we also saw how, in two dimension, the physics underlying superfluidity is described by the BKT theory. Indeed, to reach the superfluid regime, we need temperatures lower than the BKT critical temperature

$$T_{BKT} = \left(\frac{\hbar^2}{2\pi m k_B} \right) \frac{n}{\ln(C/\tilde{g})}. \quad (2.18)$$

Low temperatures are also required to further suppress molecules losses, since T enters also in the Eq. 2.17 through $E_c \sim k_B T$, and to maximize their production efficiency, increasing the phase space density.

This picture gets more complicated when we consider the role of the density. Indeed, T_{BKT} is directly proportional to the gas density n , as are the loss rates, given by βn . Therefore, the lifetime of the molecules is inversely proportional to the density. For these reasons, one has to carefully choose a density high enough to have T_c compatible with temperatures already demonstrated in one-dimensional lattices [7], but low enough to have lifetimes long enough (typically 100 ms) to allow performing experiments on the system. Intuitively, density strongly depends on the trapping frequencies of the optical lattice we will use to realize the two-dimensional system,

therefore the choice ultimately concerns the lattice parameters we introduced in Section 2.1.

In order to build our model we will consider first the BKT critical temperature. Given an interaction strength \tilde{g} and the two-dimensional density n of the gas, T_c changes according to Eq. 2.18. As we saw in Chapter 1, this expression is valid for infinite systems with only contact interactions, nevertheless minor corrections due to DDIs are expected [50]. Furthermore, since the finite size of the system typically increases the critical temperature [16], estimations using Eq. 2.18 can be thought as a lower bound for the real system.

A rough estimation of the two-dimensional density can be given neglecting the kinetic energy with respect to the interactions in the time independent Gross-Pitaevskii equation, using the so-called Thomas-Fermi approximation

$$n(r) = |\Phi(\mathbf{r})|^2 = \frac{\mu - U_{ho}(r)}{g}, \quad (2.19)$$

where μ is the chemical potential, $g = \frac{\hbar^2}{m} \tilde{g}$ is the interaction coupling constant and U_{ho} is the radial trapping potential

$$U_{ho}(r) = \frac{1}{2} m \omega_r^2 r^2. \quad (2.20)$$

Note that m could be either the mass of Dy atoms or Dy₂ molecules. From Eq. 2.19 we see that at the trap center ($U_{ho} = 0$) the density is $n_0 = \mu/g$, where the chemical potential can be calculated requiring a fixed particle number N

$$N = 2\pi \int_0^{R_{TF}} n(r) r dr = \frac{\pi R_{TF}^2}{2b} \mu \quad (2.21)$$

Here the upper bound of the integration interval is the Thomas-Fermi radius, defined as the distance at which the system density vanishes, $R_{TF}^2 = \frac{2\mu}{m\omega_r^2}$.

Since we expect the most part of condensed atoms sitting within the trap center, we can reasonably take for our calculations a constant density $n \approx n_0$

$$n \approx \sqrt{\frac{m\omega_r^2 N}{\pi g}} \quad (2.22)$$

which obviously depends on the radial trap frequency and the total atom number of particles in each lattice site.

To start putting some numbers in our model, let us assume $w_0 \sim 200 \mu\text{m}$ for the waist of the lattice beam with a power $P = 2 \text{ W}$. These are reasonable values which will be then discussed at the end of this chapter. With $\lambda = 1064 \text{ nm}$, Eq. 2.7 gives $\omega_r = 2\pi \times 26 \text{ Hz}$ and $\omega_z = 2\pi \times 22 \text{ kHz}$ for both atoms and molecules. Indeed, molecules have twice the polarizability of single atoms and they feel a lattice twice as deep, nevertheless, having twice the mass, the harmonic oscillator frequencies

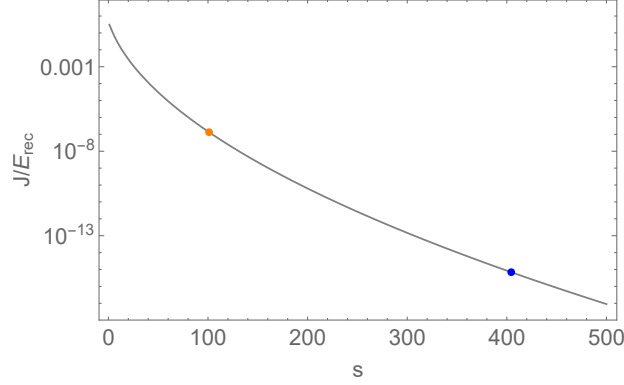


Figure 2.4. Tunneling rate as a function of the lattice depth s . The blue and orange dots respectively corresponds to Dy atoms and Dy₂ molecules trapped in a lattice with $\omega_r = 2\pi \times 26$ Hz and $\omega_z = 2\pi \times 22$ kHz.

are the same of the atomic case. For similar reasons, molecules have half the recoil energy of Eq. 2.9 of atoms, therefore, as reported in Fig. 2.4, their tunneling energy is reduced by a factor 4. Note that, in order to go as closer as possible to a true 2D system, we want $J \rightarrow 0$. Indeed, in the presence of this relatively strong confinement along the lattice direction \mathbf{z} , the tunneling of both atoms and molecules between adjacent lattice sites (or layers) can be neglected. In this configuration each layer has to be considered as an isolated two-dimensional system with N particles. This number, that enters directly in Eq. 2.19 can be roughly estimated geometrically. Indeed, with a typical number of atoms $N_{TOT} = 3 \times 10^4$ in the 3D trap actually used in our experiments and assuming the size of the cloud along the lattice direction being $\sim 5 \mu\text{m}$, loading a lattice with $d_\ell = 0.532 \mu\text{m}$ means filling about 10 layers with $N = 3000$ atoms per layer. With unity atoms-to-molecules conversion efficiency, we will have $N/2$ molecules per layer, corresponding to a density of about $2 \times 10^9 \text{ cm}^{-2}$.

In Figs. 2.5 and 2.6 we can see the calculated values of T_c using Eqs. 1.32 and the parameters discussed above. This analysis gives a critical temperature of about 50 nK for atoms and 30 nK for molecules. As pointed out at the beginning of this section, these temperatures are then slightly lowered by dipolar interactions so, in order to obtain a large enough condensed fraction, we can set a target temperature around $T_c/2$ in the molecular case. This brings us to a target temperature of about $T_T = 10$ nK corresponding to a density of $n_T = 6.5 \times 10^8 \text{ cm}^{-2}$. At this level it is important to note that, by changing ω_z , i.e. the incident power of the lattice beam, we can modify the interaction strength \tilde{g} , but this changes T_{BKT} only slightly. On the other hand, the dependence of T_{BKT} on density or N , which actually depend on ω_r , is much steeper.

Having set the target density n_T for the molecular system, we now consider its stability against the three body recombination processes described in Section 1.2. The first thing we want to check is the consistency of the Quantum Threshold model used in [41], calculating β for Dy₂ in the three-dimensional case. Using Eq. 1.21,

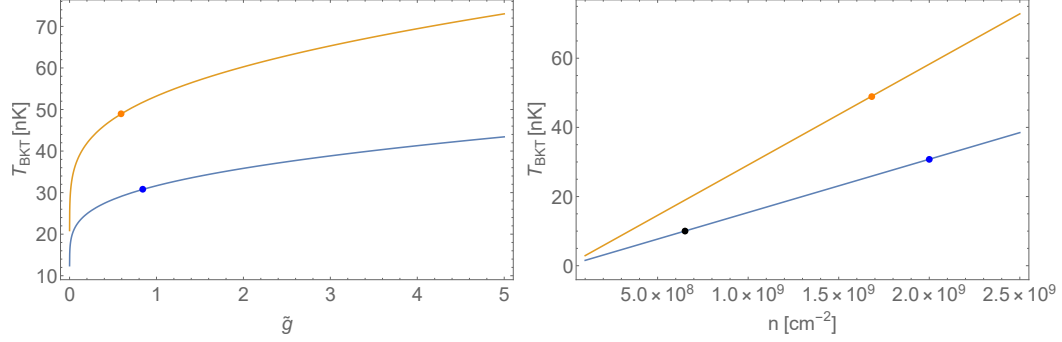


Figure 2.5. BKT critical temperature, calculated using Eq. 1.32, plotted as function of the interaction strength \tilde{g} (left) and the two-dimensional density n (right). Blue and orange curves respectively correspond to 3000 ^{162}Dy atoms and 1500 $^{162}\text{Dy}_2$ molecules. In the left plot, densities (calculated with Eq. 2.22) are $1.7 \times 10^9 \text{ cm}^{-2}$ for atoms and $2.0 \times 10^9 \text{ cm}^{-2}$ for molecules. In the right plot, \tilde{g} given by Eq. 1.29 is 0.60 for atoms and 0.84 for molecules. The black dot in the second plot indicates the density at which T_{BKT} reaches 10 nK in the molecular case.

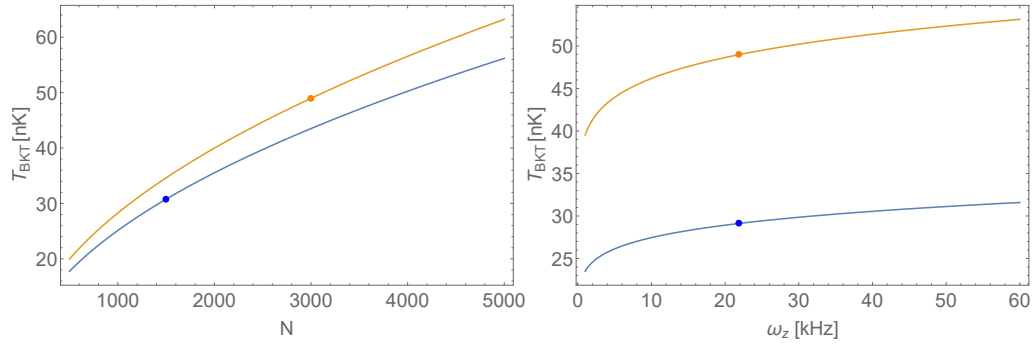


Figure 2.6. BKT critical temperature, calculated using Eq. 1.32, plotted as function of the particle number N (left) and the trap frequency ω_z (right). Blue and orange curves respectively correspond to ^{162}Dy atoms $\tilde{g} = 0.60$ and $^{162}\text{Dy}_2$ molecules $\tilde{g} = 0.84$. In the left plot, the vertical trap frequency is 22 kHz. In the right plot, the temperatures are calculated for 3000 atoms and 1500 molecules.

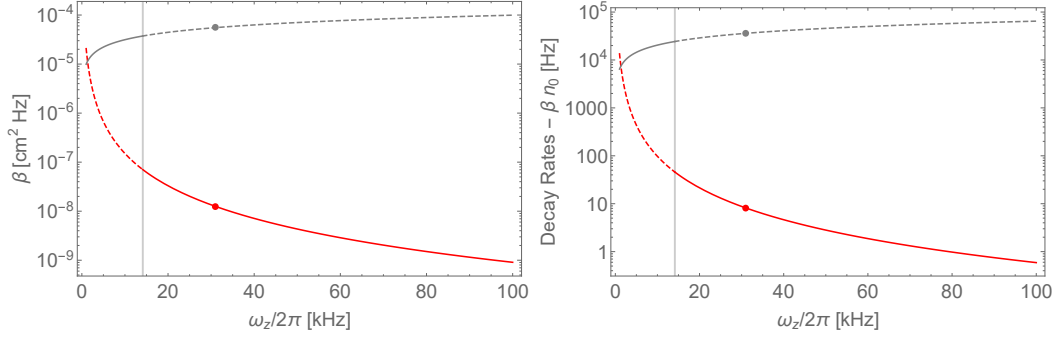


Figure 2.7. Loss rates as a function of the vertical trap frequency, calculated using the quasi-2D model in Eq. 1.22 (gray) and the 2D model in Eq. 2.17 (red). The gray vertical line correspond to the value of ω_z which gives $\ell_z \sim a_{dd}$, which separates the validity interval (solid lines) of the two models. With our trap frequency, marked with dots on both curves, we obtain $\beta^{2d} = 1.25 \times 10^{-8} \text{ cm}^2 \text{ Hz}$. With $n_0 = n_T \sim 6.5 \times 10^8 \text{ cm}^{-2}$ this gives a loss rate of $\sim 8 \text{ Hz}$. In these calculations $C_6 = 1890 \text{ a.u.}$ [29], the molecular magnetic moment is $\mu(\text{Dy}_2) = 2\mu(\text{Dy}) - 0.13\mu_B$ [33] and $E_c/k_B = 10 \text{ nK}$.

we can estimate a $\beta^{3D} = 6.22 \times 10^{-10} \text{ cm}^3 \text{ Hz}$ where, as expected the dipolar term weighs about ten times the van der Waals one, confirming that we are deeply in the dipolar collision regime. The loss rate in this case is about $\beta^{3D} n_T \sim 10 \text{ kHz}$, therefore the molecular system in three-dimensions has a lifetime of about 0.1 ms which is definitely too short to perform any type of experiment.

To estimate the loss rate in two-dimension we can use both the re-scaled 3D model (quasi-2D) in Eq. 1.22 or the 2D model in Eq. 2.17 described in [49], depending on the oscillator length ℓ_z we choose for the two-dimensional trap. While the quasi-2D model is valid for $a_{dd} \ll \ell_z$, the 2D model starts giving a good approximation of the actual rate for $a_{dd} \sim \ell_z$ [41], which corresponds to our case, since $a_{dd}/\ell_z \sim 1.5$ for Dy_2 molecules. The results of our calculations are reported in Fig.2.7, where the vertical line marks the trapping frequency $\tilde{\omega}_z$ where the 2D model start to be effectively valid. Differently from the quasi-2D model, in which β grows with the square root of ω_z , in the 2D we can see a strong suppression in loss rates, for increasing trap frequencies. With our values of ω_z we obtain a $\beta^{2D} n_T \sim 8 \text{ Hz}$, or equivalently a lifetime of about 125 ms. This timescale is now acceptable, because it is comparable with the duration of typical experiments in quantum gases, like the one investigating the supersolid properties of dysprosium performed in our lab [47], where the supersolid state survives for about 100 ms.

At this point, it is both interesting and useful to compare the results of our simulations with the experimental values obtained in [17], where the loss rates of weakly bound Er_2 molecules have been investigated. Erbium has about the same atomic mass of dysprosium, but a half its dipolar length, due to a weaker magnetic dipole moment $\mu(\text{Er}) \approx 7/10 \mu(\text{Dy})$. Using Eq. 2.17 we find

$$\frac{\beta^{2D}(\text{Er}_2)}{\beta^{2D}(\text{Dy}_2)} \sim \frac{e^{-2}}{e^{-2(2)^{2/5}}} \approx 2 \quad (2.23)$$

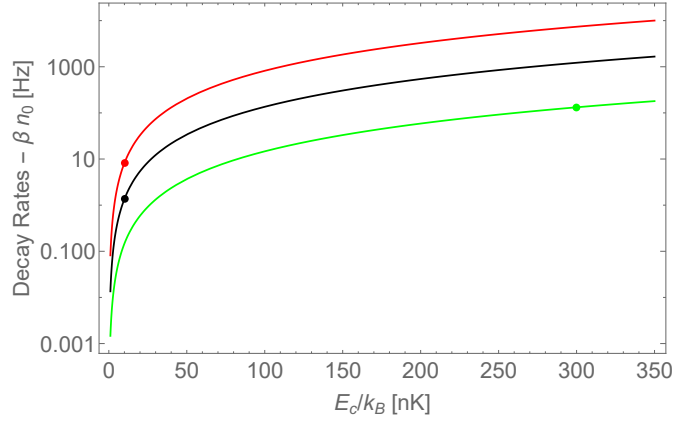


Figure 2.8. Loss rates as a function of the temperature. The red line corresponds to the previous calculations carried out for Dy₂ in a trap with $\nu_z = 22$ kHz. The red dot is equivalent to the one in Fig. 2.7. The black line corresponds to Dy₂ confined in a trap with $\nu_z = 69$ kHz, which has been calculated using Eq. 2.7 with the same $w_0 = 200 \mu\text{m}$ and $P = 10W$. The green line corresponds to Er₂ confined with the same vertical trap frequency of [17] $\nu_z = 31$ kHz. Red and black dots are at $E_c/k_B = 10$ nK, giving respectively a lifetime of ~ 125 ms and ~ 0.7 s. The green dot is instead at $E_c/k_B = 300$ nK, where the lifetime are of the order of 10 ms. In the dysprosium case (red and black) density is $n = 6.5 \times 10^8 \text{ cm}^{-2}$, while in erbium (green) we used $n = 3.8 \times 10^7 \text{ cm}^{-2}$.

therefore, β^{2D} for Er₂ is about twice the one calculated in our case, meaning that the lifetime is halved. On the other hand, in the experiment with erbium, the molecular system has a density of $3.8 \times 10^7 \text{ cm}^{-2}$, which is about 20 times smaller than the one used in our calculations. Since the loss rate is linear in density this gives an effective improvement of the system lifetime of the same factor. Nevertheless, the system temperature plays a much important role. As we said, in dipolar regime van der Waals interaction slightly affect the loss rates, which depends only from the attractive part of DDI. When the latter is suppressed, as in 2D, the system is mainly repulsive but thermal effects can still bring molecules close to each other, producing losses. This effect enters Eq. 2.17 through $E_c^2 \sim (k_B T)^2$. The temperature of the molecular sample of erbium is around 300 nK, about 30 times our target temperature. This means a loss rate about 1000 times greater in the Er₂ case. The overall effect of a_{dd} , density and temperature gives a lifetime of about 20 ms for the experiment reported in [17]. Based on this comparison, we clearly see how weakly bound molecules of dysprosium at very low temperatures represent a better candidate to explore the strongly dipolar regime.

To sum up the results of our calculations, we have identified a promising set of parameters for the realization of a strongly dipolar superfluid in the quasi-2D layers of an optical lattice. The specific parameters we have found are the following:

- temperature $T = 10$ nK;
- density $n = 6.5 \times 10^8 \text{ cm}^{-2}$;
- vertical frequency $\omega_z = 2\pi \times 22$ kHz;

- radial frequency $\omega_r = 2\pi \times 26 \text{ Hz}$;
- lifetime $(\beta n)^{-1} = 125 \text{ ms}$.

These parameters can be realistically obtained in the current experimental setup. Nevertheless, it is useful to consider how possible slight variations of the parameters would change the results. Let us consider once again the system density, which is maybe the most problematic estimate given, since it depends from the number of atoms per layer. Indeed, this number has been obtained from geometrical arguments instead of a numerical simulation of the real ground state density of the gas loaded in the lattice (which is outside the scope of this work). Moreover, n_T depends on the molecules association efficiency, which we assumed to be unity. If the density of the system is smaller than n_T we will have a lower critical temperature. This effect can be compensated focalizing the beam on a smaller waist, effectively increasing ω_r and, therefore, the two-dimensional density. On the other hand, if the latter is larger than n_T , we have to deal with more losses. In this case, we can increase ω_z , hence the confinement along the lattice, using more laser power. Note that in our estimates, we have chosen $P = 2 \text{ W}$, but this can be realistically increased to at least $P = 10 \text{ W}$, using a dedicated laser source. Since T_{BKT} has a smooth dependence on ω_z , increasing the confinement modifies only slightly the critical temperature, affecting only the loss rates. Therefore it is also possible to increase both the density (reducing the lattice beam waist) and ω_z (increasing P) to get larger critical temperatures with a minimal cost in losses. This approach can be used if the critical temperature of the real system is below the target temperature.

Another effect we did not consider in our model is the heating of the system during the adiabatic compression needed to load the lattice. Starting from the three-dimensional optical trap with a trap frequency along z of about 100 Hz , our system is then compressed in a single lattice site, where ω_z is around 10 kHz . Adiabatic compression of a thermal gas in general produces an increase of temperature. Indeed, adiabaticity implies that the particles remain in their initial quantum states, while the energy of the states changes due to the compression. Considering the population p_i of the i -th level of the harmonic oscillator along \mathbf{z} , adiabaticity implies

$$p_i = \exp \left[\frac{i\hbar\omega_z}{k_B T} \right] = \text{const} . \quad (2.24)$$

Therefore if we change ω_z by a factor of 100, also the temperature along \mathbf{z} needs to change accordingly, keeping the population p_i constant. For the equipartition theorem, this heating redistributes equally in the three spatial dimensions once the system thermalizes. This gives an actual increase of the gas temperature by a factor 30. Therefore, it is clear that one must either start from an ultracold BEC with temperature well below 10 nK , or provide cooling during the compression. This last solution can be implemented using a magnetic field gradient that lowers the trapping potential along r , letting go hot atoms out of the lattice: this however has a cost in terms of atom number. We will design the specific procedure to follow during the preparation of the experiment. One important note is that temperatures around 10 nK are routinely reached in tight optical lattices, even in 3D lattices [7],

so it should be possible to reach those levels of temperatures also in our planned experiment.

As we said in Section 2.2, another source of heating that needs to be considered is given by the light intensity noise of the lattice beams. We expect this effect to be small, if compared to losses due to collisions or non adiabatic loading of the lattice. Therefore, starting from Eq. 2.15, we can require lifetimes longer than 1 s, obtaining

$$S_{\gamma}(2\nu_{trap}) < \frac{1}{\pi\nu_{trap}^2} . \quad (2.25)$$

Assuming a constant power spectrum $S_{\gamma}(\nu) \sim S_{\gamma}(2\nu_{trap})$, the fractional rms intensity noise over a bandwidth ν_{BW} is given by

$$\gamma_{rms}^2(\nu_{BW}) = \int_0^{\nu_{BW}} d\nu S_{\gamma}(\nu) = \nu_{BW} S_{\gamma}(2\nu_{trap}) . \quad (2.26)$$

The condition in Eq. 2.25, expressed in terms of the fractional RMS intensity noise, gives $\gamma_{rms} < 2 \times 10^{-3}$ with our trap frequency.

Chapter 3

Realization of a one dimensional optical lattice

This Chapter constitutes the experimental part of my thesis, which I carried out at the Dysprosium Laboratory of CNR-INO and LENS. Here I present the building process of a new laser source which I used to realize a one-dimensional optical lattice based on the specifications I discussed in Chapter 2. In the first sections I go through the optical part of the laser set-up, following its building steps. In Section 3.4 I describe how the power of the new source is stabilized together with the control loop I realized for this task. The realization of the one-dimensional optical lattice is described in Section 3.5.

3.1 Assembling a stable laser source

In Section 2.3 we have seen the design of strongly dipolar superfluid made of dysprosium molecules, where we have highlighted the importance of the 2D confinement for the stability of the system. In particular, we have found an optimal set of parameters which gives a lifetime comparable with the one in current experiments, providing a strong confinement along the polarization axis of the dipoles, with a trap frequency $\omega_z > 20$ kHz. This can be achieved using a deep one-dimensional optical lattice, where the trap frequency along the lattice direction (see Eq. 2.7) depends essentially on power, at fixed lattice spacing. For this reason, building a laser source with high power is really important.

The present section summarizes the assembling process of this laser source, which I realized personally for Dysprosium Laboratory. Before jumping to the technical aspects and start to follow the building steps in chronological order, I would like to present the main idea behind this design, focusing on its general features.

This laser source has a wavelength of 1064 nm, far from the dysprosium resonances, and a peak output power of about 15 W, which is enough to build an optical lattice with $\lambda/2$ spacing and $\omega_z \sim 70$ kHz (corresponding to a power of 10 W focused on 200 μm). As sketched in Fig. 3.1, the set-up for this laser can be divided in three main

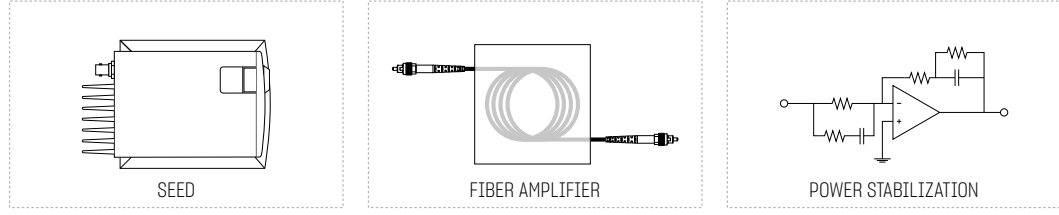


Figure 3.1. Block diagram of the laser source set-up.

sections. The laser seed and a fiber amplifier constitute a so-called Master Oscillator Power Amplifier (MOPA) whose power is then stabilized by an appropriate control loop. The seed is a Mephisto-S ultra-narrow linewidth laser with a wavelength of 1064 nm and about 200 mW of output power. This is coupled with a NUA-1064-PD-0015 double stage fiber amplifier that generates an output power from roughly 1.5 W up to 15 W, controllable through the amplification factor of the second stage. Once the output power level has been chosen, power stabilization is achieved using a PI control loop with feedback provided by a single pass Acousto-Optical Modulator (AOM).

One of the main advantages in using a fiber amplifier resides in its compactness, that allows us to mount it directly on top of the seed, saving lots of precious space on the optical table. The resulting optical scheme of the MOPA is sketched in 3.2. We have built the seed level on a breadboard, on top of which we have placed the amplifier in direct contact with its cold plate (water cooled). Seed light is injected in the amplifier through a single mode optical fiber, properly coupled using a single lens. At the output, the amplifier has its own fiber (roughly 1 m long) that ends with an optical isolator clamped to the main optical table. Here sits the last section of the set-up, as sketched in Fig. 3.3. The first diffraction order from the AOM is sampled using a combination of two polarizing beam splitters (PBS1 and PBS2) and focused on a photodiode. To achieve power stabilization, we used a PI controller that compares the photodiode voltage with a reference value, producing an error signal that feeds into the AOM driver varying its diffraction efficiency, hence the power on the first diffraction order.

This mechanism is used both to control the power during the adiabatic loading of the lattice from the starting three-dimensional optical trap in which the dysprosium BEC is held, and to prevent the heating effects due to intensity noise.

3.2 Seed Laser

The system seed is a compact Nd:YAG based laser with a measured output power P_{seed} of about 230 mW. The outgoing beam is astigmatic and elliptical, with w_{0x}/w_{0y} of about 1.35, and quite divergent. For this reason, to avoid vignetting effects we put the optical isolator (see bottom panel in Fig. 3.2) directly in front of the laser head. The isolator has an extinction ratio larger than 95% and transmits about 80% of the input power. Therefore the power P_0 we need to couple into the optical fiber

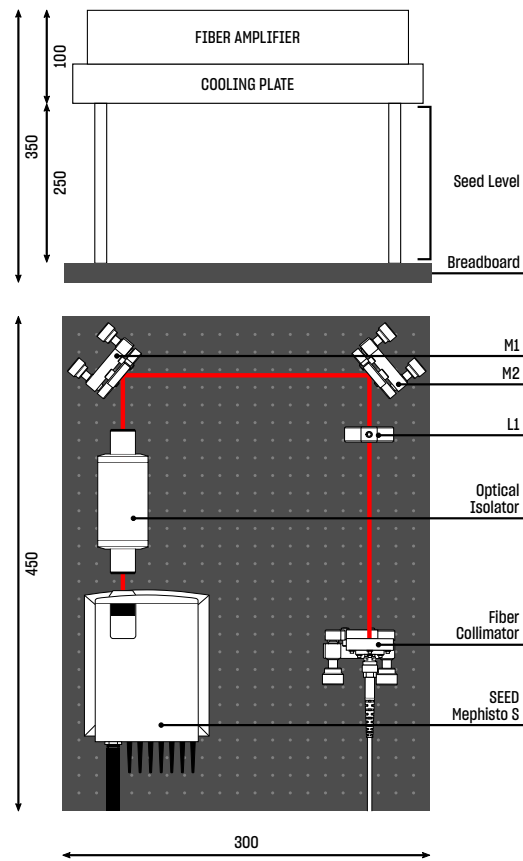


Figure 3.2. Side view of MOPA and top view of the seed level (not-to-scale). Length are in mm.

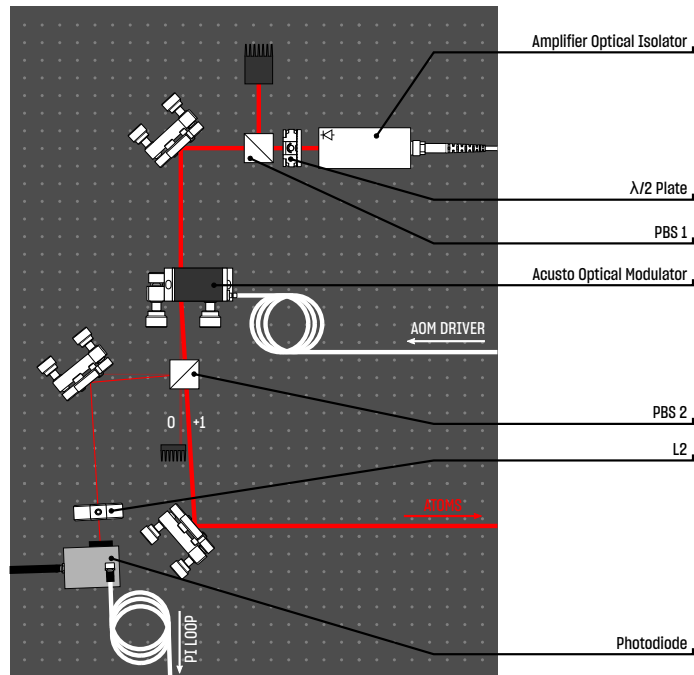


Figure 3.3. Top view of the optical scheme for the power stabilization loop (not-to-scale).

is around 190 mW. After the isolator, a couple of mirrors allow to adjust the beam height and inclination with respect to the optical table.

A summary of the main features of the seed is given in Tab. 3.1. The details about how these parameters are defined can be found in Appendix A, together with a brief review about gaussian beams propagation. The description of the experimental measures for the beam analysis is given in the next paragraph.

Analysis of the beam profile

In order to have high efficiencies in coupling seed light with the input fiber of the amplifier, we first need to characterize the seed beam and choose the right focal length for the lens L1 (see Fig. 3.2). To obtain the beam waist and its location we captured the beam intensity profile with a CCD camera at different positions along the optical axis of the system. As one can see in Fig. 3.4, each image exhibits a two-dimensional gaussian profile, well described by Eq. A.19. However, to lighten the complexity of the non-linear model used to fit the images, we performed two one-dimensional regressions along the vertical and horizontal directions, using

$$g(x) = A \exp\left(-\frac{2(x-x_0)^2}{w^2}\right) + B \quad (3.1)$$

where A , x_0 and B are respectively the amplitude, the position of the intensity maximum and an additive constant, while w is the spot size of the beam measured in pixels. To reduce the effects of noise and multiple reflections on the camera sensor, data are previously binned in both directions. For a given direction, for example the vertical one, only the central slice of the image is considered and integrated along the horizontal direction to obtain a one-dimensional data set, that can be fitted with Eq. 3.1.

This procedure is repeated for all the images corresponding to different positions along the beam propagation axis, storing the values of w and converting them in μm using the following relation:

$$w [\mu\text{m}] = w [\text{px}] \times \text{bin size} [\text{px}] \times \text{pixel size} [\mu\text{m}] . \quad (3.2)$$

Table 3.1. Seed laser features

wavelength		λ	1064 nm
output power	before OI	P_{seed}	$230 \pm 10 \text{ mW}$
	after OI	P_0	$190 \pm 10 \text{ mW}$
waist size	horizontal	w_{0x}	$179 \pm 20 \mu\text{m}$
	vertical	w_{0y}	$133 \pm 16 \mu\text{m}$
waist location	inside laser head	z_0	$-60 \pm 10 \text{ mm}$
divergence		θ	$\sim 2 \text{ mRad}$
quality factor		M^2	~ 1.2

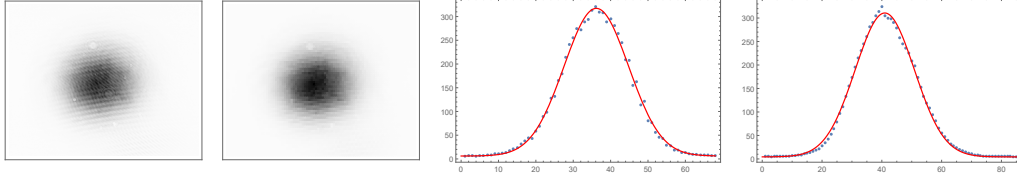


Figure 3.4. Typical images of the beam intensity profile and gaussian fit. From left to right: original image captured on CCD camera, binned image (bin size is 15×15) and gaussian fits along y and x direction.

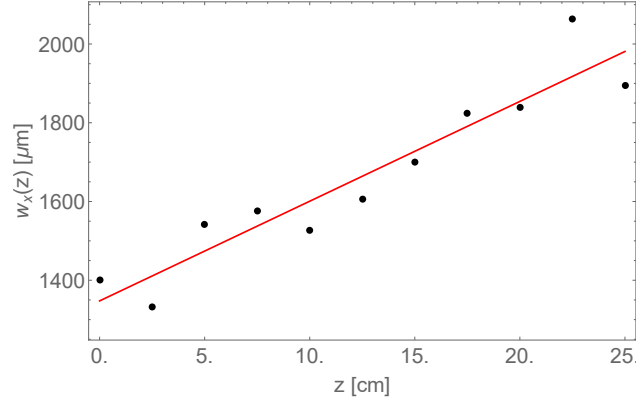


Figure 3.5. Spot size in the horizontal direction as a function of the position along the optical axis. Horizontal axis is referenced to the position of the first measured spot size, which lies ~ 60 cm far from the waist location. For this reason the best fit curve (red) is essentially a straight line.

Note that, the CCD camera used for these measures (Thorlabs DCC1545M) has 1280×1024 pixels with a pixel size of $5.2 \mu\text{m}$, hence a minimum diameter of about 5.3 mm . This puts a limit on the maximum spot size that can be measured, without vignetting effects due to beam divergence. Furthermore, we need to filter out most of the power, avoiding to overexpose the sensor during measurements. This can be done putting directly after the mirror M2 a $\lambda/2$ plate with a polarizing beam splitter that transmits only 20% of P_0 . If needed, additional filtering can be provided using reflective neutral density filters, mounted on the sensor.

The measured spot size as a function of the position is described by Eq. A.8. To set a suitable fit function, we combine the latter with the definition A.6 of the Rayleigh length, obtaining:

$$w(z) = \left[w_0^2 + \frac{(z - z_0)^2 \lambda^2}{\pi w_0^2} \right]^{1/2} \quad (3.3)$$

where w_0 is the beam waist.

The results for both horizontal and vertical waists are summarized in Tab. 3.1, where z_0 is the mean value of the fit results z_{0x} and z_{0y} , referenced to the laser head. It is important to note that uncertainties on the waist locations obtained

from the fitting method explained above are quite large ($> 10\%$) due to the fact that we are measuring at $z \gg z_R$. To have a better estimation of z_0 , we can place a positive lens with focal length f at a distance $d \sim f$ from the presumed waist location, obtaining a nearly collimated beam: varying d and observing what happens to the beam divergence, one can find a range for the waist location with higher accuracy.

One aspect of this measurement technique is the lower accuracy along the horizontal direction, that is clearly visible in Fig. 3.4. This is due to the image broadening eventually introduced when the camera is tilted with respect to the propagation axis. For this reason, both the beam astigmatism and roundness could be slightly overestimated.

Coupling Laser into a single mode fiber

To couple the seed light into the amplifier we use a single mode polarization maintaining fiber (Thorlabs P3-1064PM-FC) optimized for 1064 nm. Using a suitable collimator (OZ Optics HPUCO-23-1064-P-6.2AS) with an aspheric lens with 6.2 mm focal length, the seed light can be coupled into the fiber core, with a diameter of about $5.5 \mu\text{m}$. The fiber has a mode field diameter slightly larger than its core, of about $6.6 \mu\text{m}$, and a numerical aperture of 0.12.

Together with the seed, also the mode accepted by the fiber has to be analyzed in order to adapt the first to the second one. An intuitive method to do so, as sketched in Fig. 3.6, is to couple the seed light into the output port of the fiber (which, in the actual design, injects light into the amplifier) and analyze the beam coming out from the input port of the fiber (which is the one we want to couple in the first place). In this case the coupling efficiency is very low, therefore there is no need to dim the light using a PBS, and only the neutral density filters are used. Results of the beam analysis are summarized in Tab. 3.2. Thanks to the collimator on the output fiber the mode is only slightly divergent, but still astigmatic and elliptical, with a ratio between horizontal and vertical waists of 1.32 (substantially identical to the value we found for the input beam). Since fibers do not correct this aberration, the only option would be to use a suitable cylindrical lens before L1, but this is not crucial to have a working MOPA, as we will see in the next section.

At this level, we are just interested in achieving the correct waist w_f and divergence

Table 3.2. Fiber features

waist size	horizontal	w_{0xf}	$528 \pm 34 \mu\text{m}$
	vertical	w_{0yf}	$702 \pm 22 \mu\text{m}$
waist location	horizontal	z_{0xf}	$1.1 \pm 0.5 \text{ m}$
	vertical	z_{0yf}	$1.3 \pm 0.1 \text{ m}$
spot size	on collimator	w_f	$\sim 850 \mu\text{m}$
divergence	after collimator	θ_f	$\sim 0.4 \text{ mRad}$

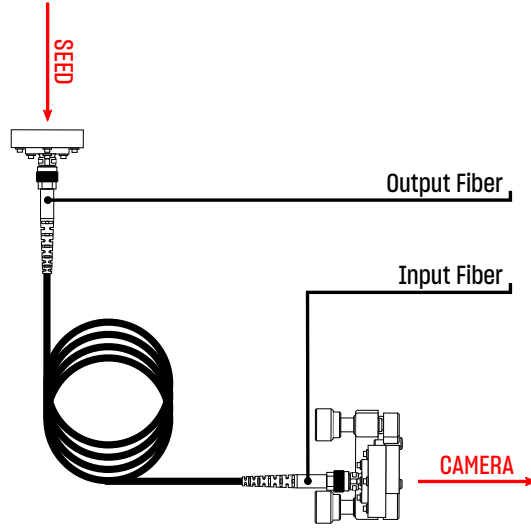


Figure 3.6. Fiber configuration for the input fiber beam analysis (not-to-scale). The output fiber is plugged into a focusing lens that allows coupling with seed light.

θ_f of the laser beam on the fiber collimator, to optimize the coupling efficiency. These two quantities can be calculated starting with values in Tab. 3.2, and using Eq. 3.3 to find w_x and w_y exactly on the collimator surface, that lies 16.2 cm from the first position of the camera. To have a good estimation of w_f we then average the calculated values. Now, the mode matching problem consists in choosing a suitable lens that transforms w_s of the seed in w_f over a total length $d_1 + d_2$, respectively separating the lens from each waist location. This problem can be solved using the transfer matrix formalism reviewed in Appendix A, and, in particular the following relations:

$$\begin{aligned} d_1 &= f \pm \frac{w_s}{w_f} \sqrt{f^2 - \tilde{f}^2} \\ d_2 &= f \pm \frac{w_f}{w_s} \sqrt{f^2 - \tilde{f}^2} \end{aligned} \quad (3.4)$$

with the quantity $\tilde{f} = (\pi/\lambda) w_s w_f$ setting a lower limit for the focal length of the beam. If instead, we set $d_2 = 0$ choosing to put the optical fiber directly after the lens, we have an equation for the optimal focal length f_{opt}

$$f_{opt} = \frac{\pi}{\lambda} w_f^2 \sqrt{\frac{w_0^2}{w_f^2 - w_0^2}}. \quad (3.5)$$

With our parameters we obtain a f_{opt} of 38 cm at a distance d_1 of 40 cm, and a focal length lower limit \tilde{f} of about 37.6 cm. This suggests to choose a 40 cm focal length for the lens L1, which unfortunately gives a total path $d_1 + d_2 \sim 1.60$ m that exceeds the breadboard dimensions. Longer focal lengths will lead in general to longer total paths, making a single lens exact mode matching impossible, without a custom lens. Nevertheless, a compromise can be found looking for a configuration in which the beam has more or less the same w_f , but is slightly convergent, with θ not

significantly different from θ_f .

The solution we adopted for this design exploits a lens with $f = 35$ cm, that couples light into the fiber with an efficiency $\leq 65\%$. This means we have an injected power into the fiber amplifier of $P_{in} \sim 120$ mW, well above the minimum power accepted by this instrument. However, the coupling efficiency remains curiously low. To explain why, we analyzed the fiber mode coming out from the output fiber, discovering abnormalities in the modal shape suggesting a damage on the fiber tip. In Fig. 3.7, we can clearly see that, while the input fiber tip shows a nice TEM₀₀ mode, the same does not happen for the output one. The origin of the damage might be a strong back-reflection from the fiber amplifier. This is a known problem in this type of amplifiers, which indeed have a protection circuit that switches them off if the back-reflection is too strong. So, in principle there should not be any power buildup at the fiber tip. Nevertheless, it may happen that before the protection circuit enters in action, some power buildup takes place, damaging the fiber. As a matter of fact, the achieved coupling was good enough to operate the amplifier, so we did not explore the phenomenon further.

3.3 Fiber Amplifier

The NUA-1064-PD-0015 is a fiber amplifier based on rare-earth-doped fibers acting in the same time as waveguide and active medium of the system. The typical dopants we can find in the fiber cores of such amplifiers are trivalent ions, such as Er^{3+} , Yb^{3+} or Nd^{3+} , depending on the lasing wavelength range requested. Our amplifier uses Ytterbium Doped Fibers (YDF), which in fact have an emission range of $1.0 - 1.1$ μm . The population inversion for Yb^{3+} atoms involves just two energy levels: $^2F_{7/2}$ (ground) and $^2F_{5/2}$ (excited). This is possible because the crystal electric field produced by the host glass of the fiber core splits each one of those two levels in a Stark manifold, where all the sub-levels are coupled by non-radiative processes. When some laser pump excites Yb^{3+} atoms, they end up in the higher sub-levels of the excited state manifold. From here, they can quickly thermalize to the lower sub-level which is (thanks to the energy gap between $^2F_{7/2}$ and $^2F_{5/2}$) a

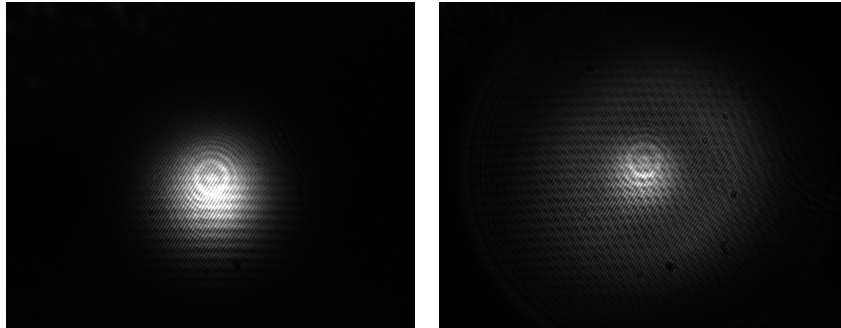


Figure 3.7. Intensity profile captured on the CCD camera for the input fiber tip (left) and the output one (right). The latter exhibits a non-gaussian profile with a ring of scattered light around a central spot, suggesting a damage on the fiber tip.

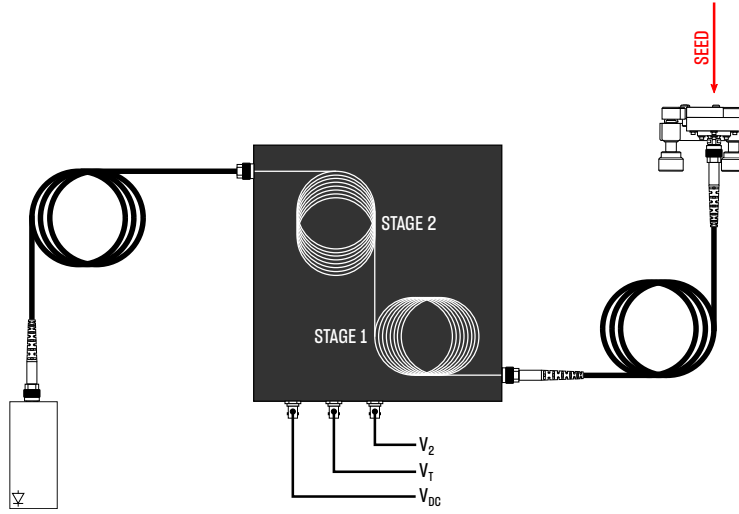


Figure 3.8. Basic scheme of a two stage fiber amplifier. The voltage signals V_{DC} , V_T and V_2 are respectively the supply voltage of the amplifier, the trigger of the first stage and the power control of the second stage. Here the input fiber is same one sketched in Fig. 3.6.

metastable state able to *store* population. Therefore, the lasing wavelength depends on the Stark splitting, which can vary depending on the host glass composition, dopants concentration and disorder.

As one can see in Fig. 3.8 this amplifier has two stages of YDFs, both with a gain $g_{amp} = +20$ dB. The first stage is triggered by a +5 V TTL signal labeled V_T and has a fixed output power, while the second stage can be adjusted by controlling the power of the pump laser via an external analog DC voltage V_2 . When the voltage V_2 is 0 V there is the minimum power (the one given by the first stage), when V_2 is 5 V, there is the maximum power. Multiple stages allow to have more control on the output power of the amplifier and, more important, to increase the damage threshold of the system. Indeed, one can use a double-clad fiber with large mode area for the second stage, reducing damages due to high intensity withing the fiber. Another important feature of this system is the optical isolator installed at the output, which prevents back scattered light to be re-amplificated causing huge damages to the doped fibers together with the seed.

In order to work properly, the system has to be powered by a DC voltage $V_{DC} = 24$ V and needs a minimum injected light power of 50 mW. In the previous section we have seen that P_{in} is around 120 mW, which is enough to make the amplifier work even with a non-optimal coupling between the input fiber and the first stage.

Characterization

We first want to measure the output power of the amplifier, testing its linearity with the control voltage V_2 . Lacking of a power meter able to manage high powers, it is useful to split the beam using the usual $\lambda/2$ plate with a PBS directly after

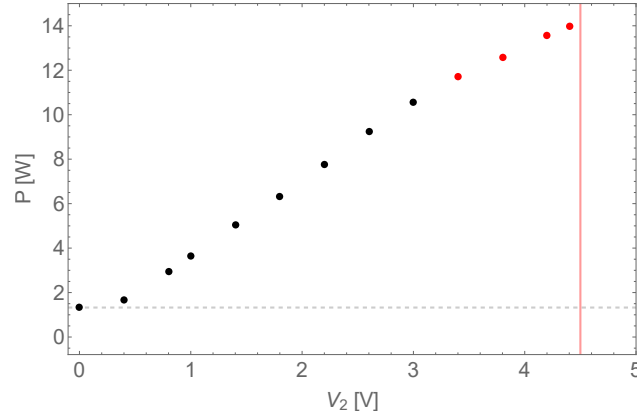


Figure 3.9. Output power (W) as a function of the voltage V_2 . The last four points are the calculated values of the total power, based on the power of the weak beam in Fig. 3.10. The horizontal gray dashed line at ~ 1.3 W corresponds to the power given by the amplifier first stage. The vertical red line at 4.5 V marks the maximum working voltage V_2 .

the amplifier isolator, having two beams with 97% (transmitted) and 3% (reflected) of the total power. At high voltages (last four experimental points in Fig. 3.9) we measure only the weak beam and calculate the power for the intense beam knowing the previous percentages. In Fig. 3.9 we can see that the total output power is linear with ~ 3 W/V slope up to 4 V, where saturation effects begin to be visible. A maximum output power of about 14.1 W is reached for $V_2 = 4.5$ V, which represents our working limit to avoid damaging the system (V_2^{MAX} is 5 V).

Another important characterization is once again the beam analysis. Due to high power we need to change a bit our filtering scheme, to prevent damaging the camera sensor and overexposing the images. As sketched in Fig. 3.10 we use a beam sampler that, with the right polarization (selected by the first $\lambda/2$ plate), reflects about 4% of the incoming light. On the reflected beam, we put our usual filtering set up and, lastly, the CCD camera. The measuring and fitting procedure is the same used in the previous sections. The results are summarized in Tab. 3.3, where the waist locations are referenced to the first position of the camera, about 30 cm far from the isolator head. The mode is basically circular and less divergent with respect to the seed one: the ratio w_{0y}/w_{0x} is about 1.08, while θ is around 1 mRad. The beam is again slightly astigmatic, with a distance between the horizontal and vertical waist locations of about 5 cm. As we will see in the next section, this is not a problem for stabilization purposes, since we are not going to focus the beam inside the AOM we use as feedback in the control loop.

3.4 Output power stabilization

In the last section of this chapter I will focus on the power stabilization of the laser source I have previously described, and on the possibility to control it over time. Indeed, controlling the light intensity of a laser with high precision is very

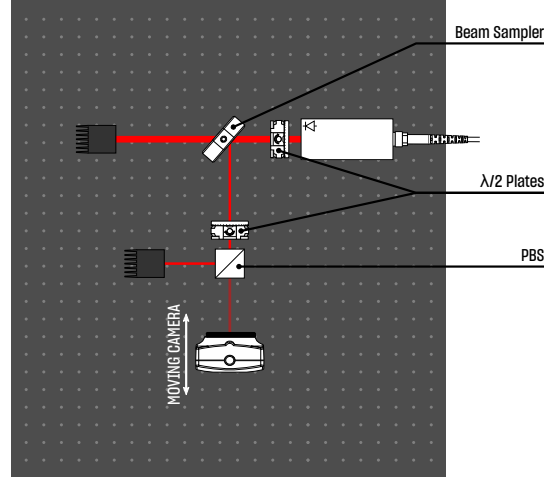


Figure 3.10. Sketch of the filtering scheme for the beam analysis.

Table 3.3. Amplified beam features

waist size	horizontal	w_{0x}	$201 \pm 3 \text{ } \mu\text{m}$
	vertical	w_{0y}	$220 \pm 3 \text{ } \mu\text{m}$
waist location	horizontal	z_{0x}	$-37 \pm 1 \text{ cm}$
	vertical	z_{0y}	$-32 \pm 1 \text{ cm}$

important when we use it to build atomic manipulation and trapping tools such as optical lattices. For example, to ensure an high efficiency loading or unloading of cold atoms in a lattice, the latter has to be adiabatically turned on and off; in addition, when we want our sample to expand freely, we need to suddenly turn off the trapping potentials. This operations happen on much shorter time scales with respect to the system lifetime, therefore a very stable and precise control mechanism is necessary. In principle, all we need to do is to control the light power coming out our system relying on an external control signal that we can set at will. In general, this requires the three basic bricks of control loops: a sensor to read the system status; a controller that compares the sensor signal to a reference one generating some sort of error value; and an actuator which provides the feedback we need to minimize that error.

For this last task, we use an AOM, that basically is a TeO_2 crystal able to diffract light and shift its wavelength in a controllable way. The AOM uses sound waves (controlled by an external radio-frequency driver) to spatially modulate the index of refraction in the crystal, which acts like a diffraction grating. It is instructive to note that, changing the amplitude or frequency of the sound wave has different effects on the diffracted light. Passing through the space modulated medium, the light undergoes constructive interference when the Bragg condition is met

$$2 \sin(\theta_m) = m \frac{\lambda}{nd} \quad m = 0, \pm 1, \pm 2, \dots \quad (3.6)$$

with θ_m and λ being the diffracted light angle and wavelength, n the index of

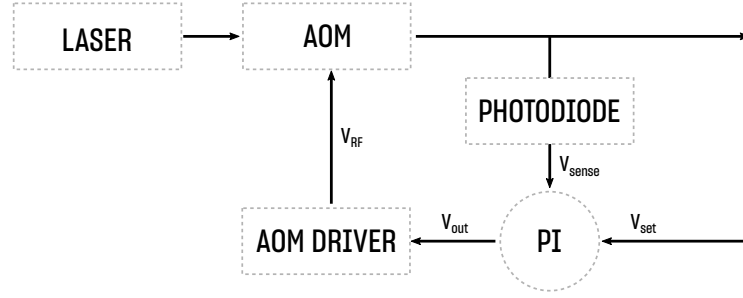


Figure 3.11. Block diagram of the control loop used for the power stabilization of the laser source.

refraction of the crystal, and d the *spacing* of the modulation, that is the wavelength of the sound wave. Therefore, changing the latter will change θ_m , deflecting the light for any $m \neq 0$. Furthermore, from a microscopic perspective, what happens when the condition 3.6 is met, is that a phonon in the medium interacts with a photon of the incoming beam changing its momentum, hence shifting its frequency. On the other hand, changing the amplitude of the sound wave will only change the peak intensity of the diffraction fringes, varying the efficiency with which the AOM *transfers* light into a certain diffraction order. This is the effect we use in our control scheme, outlined in Fig. 3.11.

As we will see, the AOM is aligned to maximize diffraction efficiency on the $m = +1$ order, that constitutes the output beam of the whole light source. Sensing is achieved using a low-noise, fast silicon photodiode, exposed to $\sim 1\%$ of the total power in the beam. This can be done exploiting a very little misalignment between the two PBS in Fig. 3.3, preventing damages to the photodiode even at maximum power. Going back to Fig. 3.11, we see that the photodiode generates a voltage signal V_{sense} that is then compared to a reference signal V_{set} by a PI controller. The latter, described in detail in the last paragraph of this chapter, produces an output signal V_{out} that is plugged into the AM bias input of the AOM driver. Closing the control loop, the amplitude modulated radio-frequency of the driver directly controls the diffraction efficiency of the AOM.

Single pass AOM alignment

Without using a lens to focus the beam into the modulator, we need to take special care about the AOM alignment. The basic idea is to exploit the divergence of the incoming beam, placing the AOM where the spot size is large enough to cover the whole working surface of the modulator, without being vignetted by the entrance hole. This will maximize the volume of crystal in which the sound wave meets the light, optimizing the diffraction efficiency. Once placed, the modulator is then slightly tilted to meet the 3.6 condition for $m = +1$. The power diffracted on this order is maximized first by tuning the radio-frequency to an optimal value, and then walking the beam with the help of a mirror, until an efficiency $\geq 85\%$ is reached. Our AOM works at ~ 104 Mhz, near to its central frequency of 110 MHz. In this

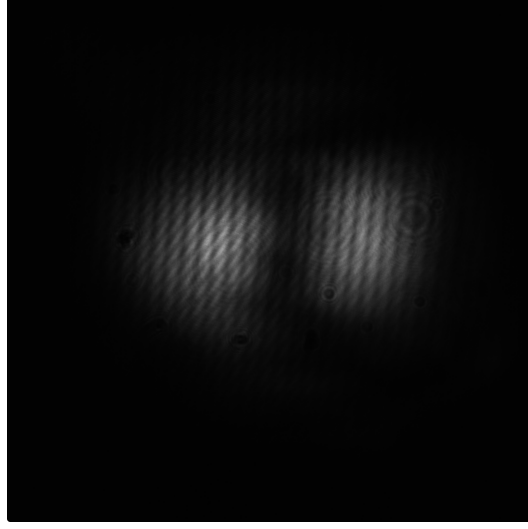


Figure 3.12. Image of the intensity profile on the AOM $m = 0$ order, exhibiting its typical *two-lobe* structure.

Table 3.4. Diffracted beam features

waist size	horizontal	w_{0x}	$208 \pm 4 \text{ } \mu\text{m}$
	vertical	w_{0y}	$222 \pm 4 \text{ } \mu\text{m}$
waist location	horizontal	z_{0x}	$-29 \pm 1 \text{ cm}$
	vertical	z_{0y}	$-24 \pm 1 \text{ cm}$

configuration we have first checked that the diffraction efficiency does not depend on the beam power, spanning through the whole range of V_2 . We also studied how the efficiency changes with the polarization of the incoming beam, finding only a weak dependence that gives $\pm 1\%$ maximum over 90° . If we observe the zero order captured by the CCD camera in Fig. 3.12 at optimal alignment, we find a *two lobe* structure with a central cut in the intensity profile that corresponds to the missing light *transferred* by the modulator in the $m = +1$ order with an efficiency of $\sim 90\%$.

We also analyzed the diffracted beam profile with the same method used in the previous sections, obtaining the results summarized in Tab. 3.4. The beam waists and locations (referenced to the first position of the camera, 35 cm far from the isolator) are compatible with the same quantities measured for the incoming beam, suggesting that the AOM does not effectively changes the beam profile but slightly shifts the position of the beam waist. Indeed, the diffracted beam remains a bit elliptical and astigmatic (as the incoming beam) with waists positioned respectively $\sim 6 \text{ cm}$ and $\sim 11 \text{ cm}$ from the isolator head.

PI control loop

A PI controller is basically an analog circuit able to generate an error signal and process it to give an output that is proportional to the error itself and to its integral

over time. In our case, the error signal is the difference between a setpoint value V_{set} (chosen arbitrarily) and the signal produced by the photodiode V_{sense} . On the left part of Fig. 3.13 we can see a typical example of the subtraction circuit generating $V_{err} = V_{sense} - V_{set}$, that is then given as input to the proportional and integral parts constituting the actual PI controller. For this simple case we can define the proportional and integral gains g_P and g_I as the ratio between the output voltage of each operational amplifier and the error signal, obtaining:

$$g_P = -\frac{R_2}{R_1} \quad (3.7)$$

$$g_I(\omega) = -\frac{1}{R_1(j\omega C_1)} \quad (3.8)$$

where j is the imaginary unit. As we see, while g_P is constant, g_I depends on the frequency ω of the error signal. The output voltage of the device is given by:

$$V_{out} = -(V_P + V_I) = +V_{err}(g_P + g_I(\omega)) . \quad (3.9)$$

Note that here we have neglected the finite bandwidth of the operational amplifiers. To take this aspect into account let us consider the more general circuit in Fig. 3.14, where the op-amp used has a bandwidth of $\Delta\omega_{BW}$. Given z_1 and z_2 as the circuit impedances, the gain is in this case [24]

$$g(\omega) = \frac{z_2}{z_1} \left[\frac{1}{1 - \frac{z_1+z_2}{z_1} \frac{1}{A(\omega)}} \right] \quad (3.10)$$

where $A(\omega)$ accounts for the finite bandwidth of the amplifier

$$A(\omega) = \frac{A_0}{1 + \frac{j\omega}{\Delta\omega_{BW}}} . \quad (3.11)$$

When $\omega \gg \Delta\omega_{BW}$, $A(\omega) \rightarrow 0$ and we have a vanishing gain from Eq. 3.10, as we expect when we exceed the amplifier bandwidth. On the other hand, when $\omega \ll \Delta\omega_{BW}$, $A(\omega) \rightarrow A_0$ and the gain is simply given by z_2/z_1 , as it is in the ideal case we considered in Eq. 3.9.

We report the gain of a typical PI controller as a function of frequency in Fig. 3.15, where we can clearly see three different regions. At high frequency the gain rapidly decreases, meaning that the system is not working: this happens when the signal frequency exceeds the bandwidth of the op-amp used in the controller. Decreasing ω we enter the region where the proportional part of the controller dominates, holding the gain constant at g_P . At low frequencies the gain grows rapidly because the integral part of the controller dominates. This means that the controller is going to stabilize the quick oscillations using the P-part while the I-part will deal with slow oscillations of the system. The frequency that marks the boundary between these two regions, is given by $\omega_C = (R_2 C_1)^{-1}$, where $g_I(\omega) = g_P$. This is equal to the characteristic frequency $\tau_{RC}^{-1} = (R_1 C_1)^{-1}$ when $g_P = 1$.

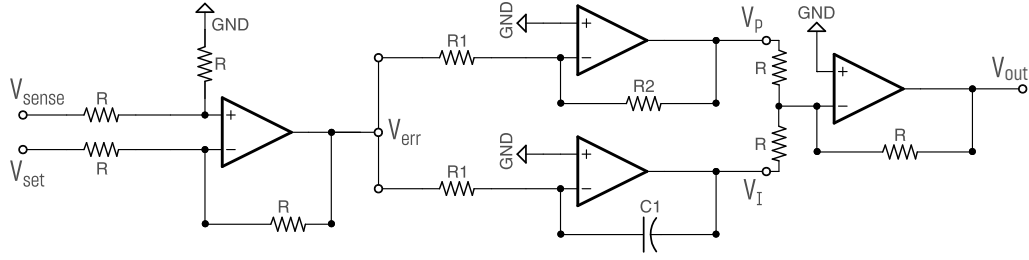


Figure 3.13. Scheme of a standard PI controller. On the left we see the subtraction circuit that produces the error signal V_{err} . In the central part, the proportional (top) and integral (bottom) circuits process the error signal producing V_P and V_I , which are summed by the last operational amplifier.

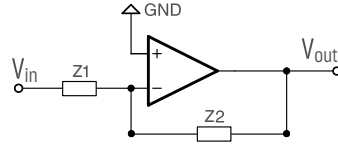


Figure 3.14. Basic scheme of an inverting operational amplifier. Here, z_1 and z_2 are generic impedances. The amplifier has a finite bandwidth, hence the gain is described by Eq. 3.10.

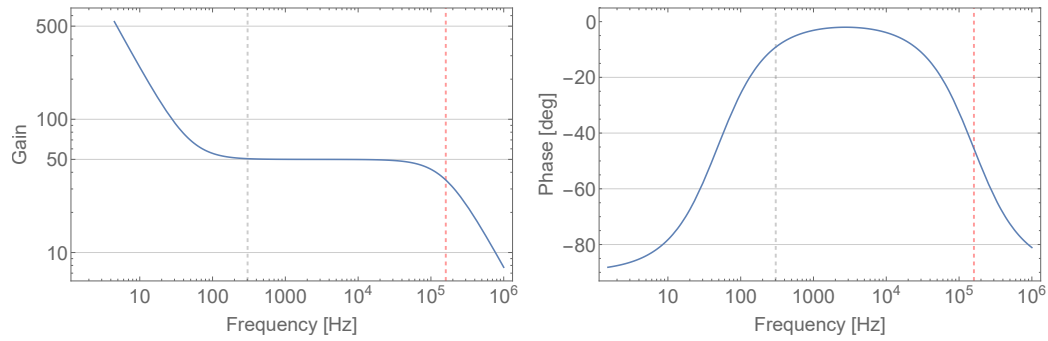


Figure 3.15. Response of a simulated PI controller. The proportional gain is 50 and the characteristic frequency of the I-part is ~ 15 kHz. The red dashed line at 160 kHz marks the cut-off frequency of the op-amp which have a gain-bandwidth product of 8 MHz. The gray dashed line at $\omega_C \sim 300$ Hz marks the limit of the constant gain region at low frequencies, where the I-part start to be dominant.

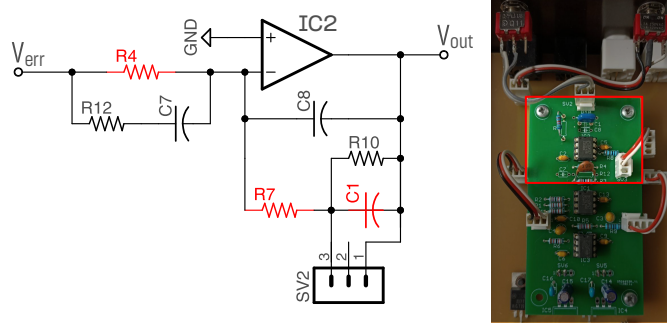


Figure 3.16. A picture of the device used to build the PI controller for the stabilization of our laser source, together with a detail of its electrical scheme. Here IC2 is the OP27 operational amplifier used for the PI part of the device. Besides IC2 and the switch SV2, only the circuit elements highlighted in red are used.

For the stabilization of our source we used a board, developed at LENS, that we adapted to serve as a PI controller. The board, depicted in Fig. 3.16, is based on three OP27 amplifiers with a gain-bandwidth product of about 8 MHz, and a zero-frequency open-loop gain A_0 of 1.8×10^6 . The first one is used for the subtraction circuit in the same configuration sketched in Fig. 3.13. The second OP27 combines the proportional and integral part of the controller, as reported in Fig. 3.16, giving the same result as the redundant scheme in Fig. 3.13. Indeed only the discrete elements highlighted in the scheme are used, therefore V_{out} can be calculated using Eq. 3.10 with $z_1 = R_4$ and $z_2 = R_7 + (i\omega C_1)^{-1}$. In this case we have

$$\frac{z_2}{z_1} = \left(\frac{R_7}{R_4} + \frac{1}{i\omega C_1} \right) \quad (3.12)$$

where we clearly recognize the proportional and integral gains defined in Eqs. 3.7 and 3.8, which we can tune by varying R_4 , R_7 and C_1 . Note that the integral part of the controller can be turned on and off using a switch that provides a short-circuit across C_1 (SV2 in the scheme). The controller could also be upgraded to a full PID circuit by simply adding R_{12} and C_7 , accounting for the derivative part. A third operational amplifier is used as a buffer for monitoring either V_{set} or V_{sense} , that can be selected using another switch.

As we said in the beginning of this section, stabilizing the power of our source is crucial to have a precise control of the light intensity over time, for example, when we adiabatically ramp-up the optical lattice, or when we suddenly want to turn it off. Another important aspect we have to take into consideration when choosing the system gains is the intensity noise, that, as we saw in Section 2.3, is a natural source of heating for the trapped system. In particular we are interested in stabilizing the noise at twice the frequency trap, which in our case means ~ 100 kHz. Since in our PI the gain-bandwidth product is 8 MHz, with $R_4 = 1$ k Ω we choose $R_7 = 50$ k Ω : in this way $g_P = 50$ and the bandwidth is nominally 160 kHz. To choose the integral time constant, we require that the typical *knee* at ω_C would be of the order of 100 Hz. Therefore we set $C_1 = 66$ nF, giving $\omega_C \sim 300$ Hz. These values are the same one used in the simulations in Fig. 3.15, so it is possible to compare the theoretical

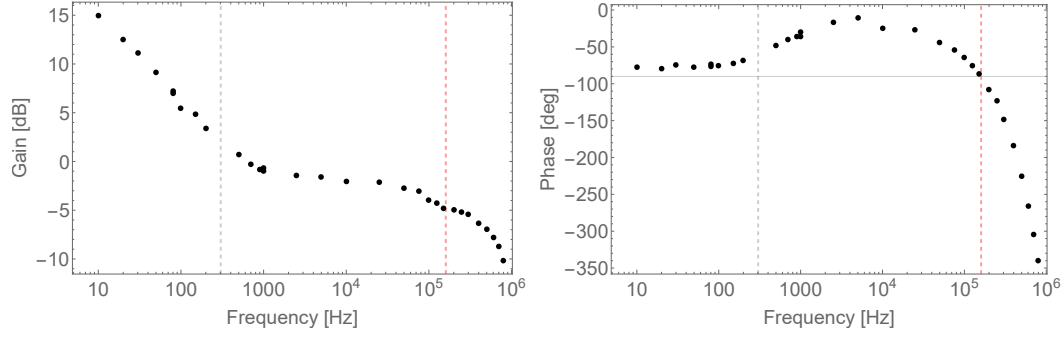


Figure 3.17. Open loop response of the control system used for the power stabilization (sketched in Fig. 3.11). Here the red and gray vertical lines corresponds to the theoretical values of ω_C and the bandwidth cut-off frequency plotted also in Fig. 3.15. The gray horizontal line corresponds to -90° .



Figure 3.18. Images of two specific measurements in Fig. 3.17, showing V_{sense} (yellow) for two different frequencies of V_{set} (blue): 1 kHz (left) and 300 kHz (right).

response of the controller with the real one. To do so, we measured the open loop response of our control system using a synthesized sine wave as set-point signal V_{set} , disconnecting the photodiode V_{sense} from the PI. For different values of the sine wave frequency ranging from 1 Hz to 1 MHz, we measured the ratio between the amplitudes of V_{sense} and V_{set} and their phase difference.

The results are plotted in Fig. 3.17. The measured gains are quantitatively different from the simulated case, since here we have also the contribution of the optical part of the feedback loop (AOM and photodiode), which apparently have no significant influence on the characteristic frequencies of the system. Indeed, the measured bandwidth and ω_C are in good agreement with the expected values. In Fig. 3.18 we can see two specific measurements respectively at 1 kHz and 300 kHz. In the first case we are near the unitary gain region, where the V_{sense} (yellow) is almost in phase with V_{set} (blue). At lower frequencies the phase begin to increase (around ω_C) due to the onset of the I-part of the controller. At high frequencies, the gain starts to decrease due to the finite bandwidth, and the two signal get out of phase. The fast variation of both gain and phase at very large frequencies is presumably due to additional impedances in the circuit, not included in our simple model.

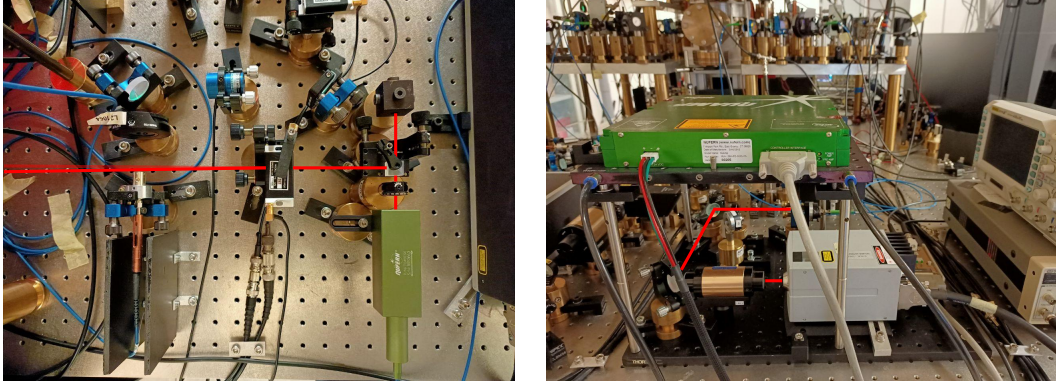


Figure 3.19. Pictures of the MOPA (right) and of the first part of the optical scheme for the power stabilization (left).

From this results we see that our device has a bandwidth large enough to reach $2\omega_{trap}$, where the intensity noise can heat the atoms or molecules sitting in the lattice. However, this is not enough to be sure that the stability conditions described in Section 2.3 are met. In particular, based on our estimations, we require the fractional rms intensity noise (over a bandwidth of 150 kHz) to be less than 2×10^{-3} in order to have lifetimes due to heating of about 1 s. Checking this specification, would require a precise measurement of the power spectrum of the intensity noise, which cannot be done with the oscilloscope available in the lab due to its limited resolution. In the future, we will carry out this measurement with a dedicated spectrum analyzer.

3.5 Building the optical lattice

In this Section I briefly summarize the realization of the one dimensional optical lattice we will use in our experiment, to trap a strongly dipolar superfluid in two dimensions. The lattice beam enters the main vacuum cell depicted in Fig. 2.2 from below, crosses the optical dipole trap where the dysprosium BEC is held, and it is back reflected by a mirror positioned outside the vacuum cell, about 25 cm from the atoms. Here I discuss the how I designed the optical setup needed to focus the beam onto the atoms, and how the laser source I have built has been integrated with the main experiment currently operating in the lab.

Since the main part of new laser source has been realized on a movable breadboard, only the stabilization of the MOPA power needed to be reconstructed on the experiment optical table. As we can see in Fig. 3.19 (right) the laser has been mounted next to the vacuum apparatus where, choosing the right position for the amplifier optical isolator, we can easily reach the lower window of the cell. In Fig. 3.19 (left) we see the first part of the laser stabilization, where the light is coupled into the AOM. Differently from the original design, sketched in Fig. 3.3, here we did not use a mirror to optimize the coupling with the AOM, instead we use directly PBS1 to reach the optimal alignment. In this case the beam diffracted by the AOM is the one reflected by PBS1, so the optical scheme of the power stabilization needed to be re-designed. As we can see from Fig. 3.20, this time the beam sampled by PBS2

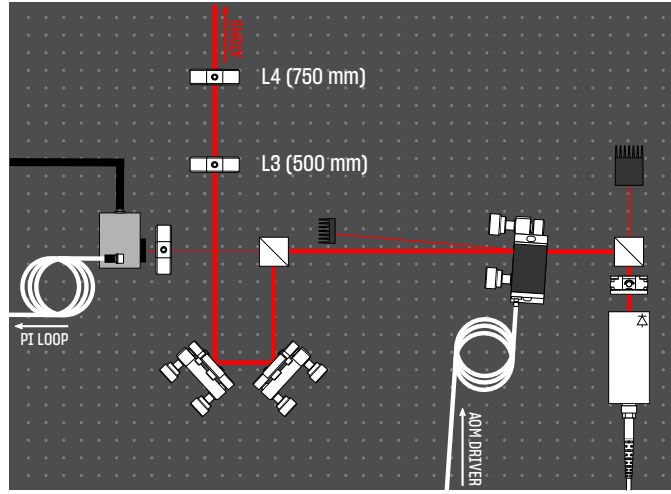


Figure 3.20. Schematic view of the optical scheme for the power stabilization of the MOPA. This is a re-design of scheme in Fig. 3.3, already discussed in this chapter. All the optical elements are the same, except from the lenses L3 and L4, which constitute part of the focusing system realized to build the lattice. Differently from the old design, here the two beam splitters are used in reflection configuration, and the AOM is aligned directly without a mirror.

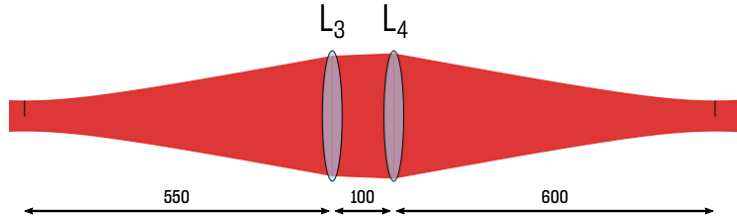


Figure 3.21. Focusing lenses L3 ($f_3 = 500$ mm) and L4 ($f_4 = 750$ mm). The black marks are the waist positions right after the isolator (left) and on the atoms (right). Lengths are in mm.

is the transmitted one, which is then focused on the photodiode using the same lens. The reflected beam, with $\sim 99\%$ of the total power is sent in the direction of vacuum apparatus using a couple of mirrors.

To realize the one-dimensional optical lattice, the beam needs to be focused on the atom cloud with the right waist, which we have found starting from the calculations carried out in Chapter 2. Since the beam waist is about $220\text{ }\mu\text{m}$ right before the AOM, and the desired waist on the atoms is about $200\text{ }\mu\text{m}$, a possible solution is to design an optical system with magnification 1. In particular we use a combination of two lenses with focal lengths $f_3 = 500$ mm and $f_4 = 750$ mm. The first one, L3, is positioned at ~ 55 cm (about its focal length) from the laser waist location, while the second one, L4, is ~ 60 cm far from the atoms. This last distance is long enough to have room for all the other optical elements needed for the MOT and imaging lasers, which also enter from the same window cell. The distance between L3 and L4 is about 10 cm, and can be slightly modified in order to slightly change the effective

focal length of the system, hence the beam spot size on the atoms. Note that this will also change the position of the waist slightly off the atom cloud, nevertheless this can be compensated by adjusting the distance between L3 and the laser waist, moving the couple of mirrors used for the alignment. The last part of the optical scheme consists on a single lens with focal length $f_5 = 250$ mm mounted directly on top of the upper window of the cell, right before the mirror, to focalize the back reflected beam onto the atom cloud, realizing the lattice.

Conclusions

In this thesis I addressed the problem of designing a strongly dipolar superfluid based on weakly bound magnetic molecules confined in two-dimensions. This new kind of dipolar system can be realized starting from a dysprosium BEC, already available in a research laboratory in Pisa, where the experimental part of this thesis has been carried out. Indeed, exploiting a Feshbach resonance, it is possible to associate pairs of atoms into weakly bound magnetic molecules, which have dipolar lengths of the same order of the inter-particle distance. Molecules are greatly unstable in three dimensions, because of the inelastic collisions at short range, which, however, are suppressed in two-dimensional systems. For this reason, this strongly dipolar quantum gas has to be prepared in two-dimensional optical traps, realized using a deep one-dimensional optical lattice, whose set-up I designed and realized in this thesis.

In the first part of my thesis I considered the relevant theoretical aspects for the study of these strongly dipolar systems, combining the fundamental role of dipolar interactions in the molecular stability with the physics of two-dimensional superfluids. I discussed the role of the system density in determining both the critical temperature of the BKT transition and the loss rates. These quantities are also linked to the strength of the two-dimensional confinement given by the optical lattice. Starting from this analysis I obtained a realistic set of parameters to be used in our experiment to realize a two-dimensional superfluid made of strongly dipolar Dy_2 molecules. I also studied the effect of possible variations of the experimental parameters, discussing how to compensate them in the real case.

From the experimental point of view, I designed and built a new light source with high power for the realization of the one-dimensional optical lattice needed for the experiment. The source is a MOPA consisting of a seed laser coupled to a fiber amplifier, giving 15 W of 1064 nm light. Besides its optical setup, I also realized the power stabilization system, based on a PI control loop. As a last part of this work, I designed and realized the optical lattice which will be used for the two-dimensional confinement. Since the main experiment was temporarily non-operative due to an ongoing replacement of the the dysprosium oven, I did not get the chance to complete the alignment of the lattice on the atoms. This, naturally constitutes the next step in the continuation of of the work started in this thesis.

Looking forward, the next important step will be to measure the lattice depth with standard techniques based on atomic diffraction by the lattice potential, checking

the agreement with the estimations I carried out in this thesis. Next, we will start experiments with the adiabatic loading of the dysprosium superfluid, aimed to verify that the resulting two-dimensional system is in the BKT regime. This can be done with time-of-flight imaging, observing the absence of free vortices below the critical temperature. Switching to molecules will require a careful characterization of the Feshbach resonances involved in the association process, together with the study of the association efficiency.

Besides these exciting experimental challenges, we also expect to observe new phenomena arising in this strongly dipolar systems. A very interesting perspective, is to study what happens when our two-dimensional gas is loaded in a regular 2D optical lattice. In this kind of experiments the interplay between the dipolar length and the lattice constant, that in strongly dipolar systems are of the same order, lead to the emergence of exotic insulator phases. In particular I am interested in studying checkerboard insulators (where the lattice filling factor is $1/2$) that are the long range counterpart of Mott insulators. While the latter have been extensively studied with both bosons and fermions in non dipolar quantum gases, the checkerboard case has never been observed experimentally and, for this reason, constitutes a fascinating objective for the future.

Appendix A

Gaussian beams

Here I will briefly cover the basics of gaussian beam propagation, recalling important definitions and setting up the notation.

A.1 Fundamental Mode

A gaussian beam is a particular solution of Maxwell's equations under the paraxial approximation, that basically discards all the plane waves solutions of Helmholtz equation, except ones with wave vector \mathbf{k} at small angles from the propagation axis $\hat{\mathbf{z}}$. The electric field of a paraxial wave can be therefore written as $\mathbf{E}(x, y, z) = \mathbf{E}_0 u(x, y, z) \exp(-ikz)$, with u being a slowly varying complex function satisfying the paraxial wave equation

$$i(2k) \frac{\partial u(x, y, z)}{\partial z} = \left(\frac{\partial^2}{\partial x^2} + \frac{\partial^2}{\partial y^2} \right) u(x, y, z) \quad (\text{A.1})$$

The lowest order solution of Eq. A.1 is in the form

$$u(x, y, z) \propto \exp \left[-i \left(p(z) + \frac{k}{2q(z)} (x^2 + y^2) \right) \right] \quad (\text{A.2})$$

where $p(z)$ represents the phase difference associated to propagation, while $q^{-1}(z)$ is the complex curvature of the beam. Substituting this solution in A.2 we can derive to differential equations for $p(z)$ and $q(z)$ which must hold for paraxial waves

$$\frac{\partial q}{\partial z} = 1 \quad \frac{\partial p}{\partial z} = -i \frac{1}{q} \quad (\text{A.3})$$

To put some physical meaning into these quantities, we first have to integrate the left of A.3 from z_0 to z obtaining A.4, then we can write the latter separating its real and imaginary part A.5 which define the radius of curvature $R(z)$ of the beam and its spot size $w(z)$

$$q(z) = q(z_0) + z \quad (\text{A.4})$$

$$\frac{1}{q(z)} = \frac{1}{R(z)} - i \frac{\lambda}{\pi w^2(z)} \quad (\text{A.5})$$

With this notation $w(z)$ measures the distance from the propagation axis at a fixed z , at which the electric field is attenuated of a factor $1/e$. The beam spot size $w(z)$ is therefore half its diameter.

We can chose z_0 to be the position on z axis in which the curvature A.5 is purely imaginary, hence $R(z_0)$ diverges, meaning that wavefronts are planes. From A.5 one can see that

$$q(z_0) = -i \frac{\pi w^2(z_0)}{\lambda} := -iz_R \quad (\text{A.6})$$

which defines the Rayleigh length for the beam. Taking together A.4, A.5 and A.6 we can derive the expression of $w(z)$ and $R(z)$, where we set $w(z_0) = w_0$ for practical reasons

$$R(z) = z \left[1 + \left(\frac{z_R}{z} \right)^2 \right] \quad (\text{A.7})$$

$$w(z) = w_0 \sqrt{1 + \left(\frac{z}{z_R} \right)^2} \quad (\text{A.8})$$

This functions are plotted in Fig. A.1, where we have called w_0 beam waist, as it is the minimum value taken by $w(z)$, and the position z_0 beam location. Another

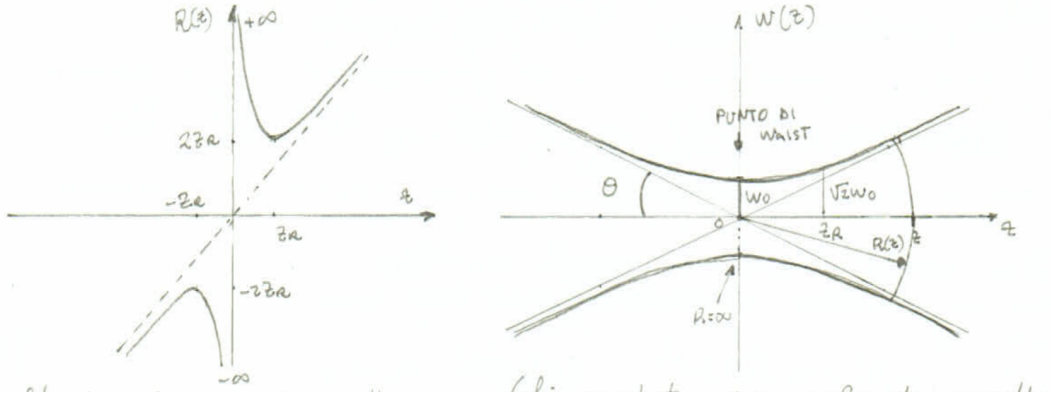


Figure A.1. Plots of the radius of curvature and the spot size as a function of z for $z_0 = 0$.

useful parameter of the beam is its divergence, that is the angle between the asymptotic value of $w(z)$ and the z axis

$$\theta = \frac{w_0}{z_R} = \frac{\lambda}{\pi w_0} \quad (\text{A.9})$$

Note that a gaussian beam is intrinsically divergent for $z > z_R$, therefore the Rayleigh length is a measure of the distance over which the beam is collimated.

Now, if we integrate the right of A.3 from $z_0 = 0$ and z , we find

$$ip(z) = \ln \left(\frac{w(z)}{w_0} \right) - i\Phi \quad (\text{A.10})$$

where $\Phi = \arctan z/z_R$ is the Gouy phase of the beam, representing the phase difference between a spherical wave and the actual paraxial wave.

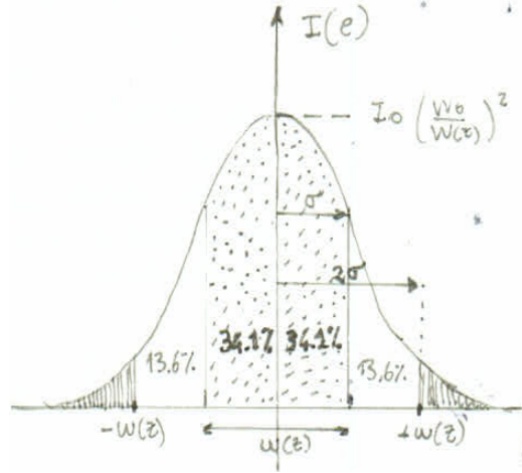


Figure A.2. Intensity profile for a gaussian beam in the plane transverse to the propagation axis.

Putting together all the previous results, the electric field for the gaussian beam reads

$$\mathbf{E}(\rho, z) = \mathbf{E}_0 \frac{w_0}{w(z)} \exp\left(-\frac{\rho^2}{w^2(z)}\right) \exp\left[-i\left(kz + \frac{k\rho^2}{2R(z)} - \Phi(z)\right)\right] \quad (\text{A.11})$$

where $\rho^2 = x^2 + y^2$ is the distance from \mathbf{z} axis. In this expression one can recognize in the factor $w_0/w(z)$ the attenuation of the electric field due to beam divergence, together with its typical gaussian profile $\exp\left(-\frac{\rho^2}{w^2(z)}\right)$ for a fixed z .

The intensity of the beam, proportional to $\langle |\mathbf{E}(\mathbf{r}, t)|^2 \rangle$, can be written as

$$I(\rho, z) = I_0 \left(\frac{w_0}{w(z)}\right)^2 \exp\left(-\frac{2\rho^2}{w(z)^2}\right). \quad (\text{A.12})$$

which again have a gaussian profile for fixed z , as sketched in Fig. A.2 with $\sigma = w(z)/2$. Even if Eq. A.12 is coherent from a mathematical point of view, it can be arranged in a more practical way introducing the beam power P , that can be easily measured with a suitable power meter. For this reason the intensity of the fundamental gaussian mode is more commonly written as

$$I(\rho, z) = \frac{2P}{\pi w^2(z)} \exp\left(-\frac{2\rho^2}{w(z)^2}\right) \quad (\text{A.13})$$

with $2/\pi w^2(z)$ being the normalization factor for a two-dimensional gaussian.

A.2 Real gaussian beams

Previous results holds only for the fundamental mode TEM_{00} , but can always be extended to higher order modes. Similarly to what one do in Quantum Mechanics,

the idea is to start with paraxial wave equation A.1 (which replace Schrödinger equation) and build a complete set of orthogonal solutions exploiting a particular symmetry of the system. Typically the cartesian coordinates are chosen, hence the amplitude u can be factorized as

$$u(\mathbf{r}) = u_x(x, z) u_y(y, z) \quad (\text{A.14})$$

and we can write two different equations for the amplitudes u_x and u_y . In order to have a more general result with respect to A.2, we look for solutions in the form of

$$\begin{aligned} u_x(x, z) &= G_x(x, z) F_x(z) \exp \left[-i \left(p_x(z) + \frac{k}{2q_x(z)} x^2 \right) \right] \\ u_y(y, z) &= G_y(y, z) F_y(z) \exp \left[-i \left(p_y(z) + \frac{k}{2q_y(z)} y^2 \right) \right] \end{aligned} \quad (\text{A.15})$$

where $G_{x,y}$, $F_{x,y}$ and $p_{x,y}$ are real functions and $q_{x,y}$ are the usual complex parameters. Independently on the functional form of $G_{x,y}$ and $F_{x,y}$, one can derive the same differential equations A.3 and expressions similar to Eq. A.5 for the curvature. The latter will be different along \mathbf{x} and \mathbf{y} axis in the case of astigmatic beams, which is the more general case. For non-astigmatic beams, we can lighten notation by dropping x and y subscripts. It is important to note that, because the curvature $q_{x,y}^{-1}(z)$ does not depend on $G_{x,y}$ and $F_{x,y}$, all the modes will have the same spot size and radius of curvature: only the transverse profile will change.

To get to the general solutions, we make now a few assumptions:

1. the amplitude in Eq. A.14 needs to be proportional to $(w_0/w(z))^2$ as for the fundamental mode, so we set

$$F(z) = \sqrt{\frac{w_0}{w(z)}}$$

2. the phase p has to be equal to the Gouy phase in Eq. A.10 multiplied by a factor which depends on the mode order

$$p(z) = - \left(m + \frac{1}{2} \right) \arctan \frac{z}{z_R} \quad m = 0, 1, 2, \dots$$

3. the G functions depends on z only through the spot size $w(z)$ as

$$G(x, z) = g \left(\frac{\sqrt{2}}{w(z)} x \right)$$

with the same expression for $G(y, z)$.

Substituting back in the paraxial wave equation will give us a differential equation for the functions $g(x, z)$ and $g(y, z)$ having Hermite polynomials as solutions. Labeling with m the increasing order of the Hermite polynomial \mathcal{H}_m , we find

$$u_m(x, z) = u_0 \sqrt{\frac{w_0}{w(z)}} \mathcal{H}_m \left(\frac{\sqrt{2}}{w(z)} x \right) \exp \left[-i \left(p_m(z) + \frac{k}{2q(z)} x^2 \right) \right] \quad (\text{A.16})$$

and the same expression for $u_n(y, z)$. This result holds also for astigmatic beams, re-introducing two different waists w_{0x} and w_{0y} along the two directions. The resulting electric field can be written as

$$\begin{aligned} \mathbf{E}_{m,n}(\mathbf{r}) = \mathbf{E}_0 \frac{w_0}{w(z)} \mathcal{H}_m \left(\frac{\sqrt{2}}{w(z)} x \right) \mathcal{H}_n \left(\frac{\sqrt{2}}{w(z)} y \right) \times \\ \times \exp \left(-\frac{\rho^2}{w^2(z)} \right) \exp \left[-i \left(kz + \frac{k}{2q(z)} \rho^2 - \Phi_{m,n}(z) \right) \right] \end{aligned} \quad (\text{A.17})$$

with $\Phi_{m,n}(z) = (m + n + 1) \arctan z/z_R$ being a generalized Gouy phase and $m, n = 0, 1, 2, \dots$ positive integers labeling the increasing mode order.

This equation describes the so-called Hermite-Gauss Transverse Electromagnetic Modes, indicated as TEM_{mn} . Even if any given monochromatic distribution of light will be a linear combination of these modes, a practical way to describe a real beam is to compare its actual waist and divergence with the parameters of an ideal TEM_{00} mode. To do so, we define M quality factor of the beam as

$$M^2 = \frac{\tilde{w}\tilde{\theta}}{w_0\theta_0} = \frac{\pi}{\lambda} \tilde{w}\tilde{\theta} \geq 1. \quad (\text{A.18})$$

An increasing M means that more higher order modes are contributing and less likely the beam will be well described by the intensity profile in Eq. A.13. Typical solid-state lasers have M^2 between 1.5 and 2.

For astigmatic beams with M^2 low enough, we can generalize Eq. A.13 obtaining:

$$I(x, y, z) = \frac{2P}{\pi w_x(z) w_y(z)} \exp \left(-\frac{2x^2}{w_x(z)^2} - \frac{2y^2}{w_y(z)^2} \right) \quad (\text{A.19})$$

A.3 Propagation with transfer matrices

In direct analogy with spherical wavefronts, the propagation of gaussian beams can be calculated using the transfer matrices formalism. These matrices are 2×2 matrices (known also as ABCD matrices) representing the optical system in which the beam is propagating, transforming the complex curvature of the beam as follows

$$q' = \frac{Aq + B}{Cq + D} \quad (\text{A.20})$$

where A , B , C and D are the element of the transfer matrix, while q' and q are respectively the final and initial values of the beam curvature. The most useful aspect of this formalism, is that any composite optical system can be described as a matrix M_{TOT} , which is the product of single matrices M_i representing elementary subdivisions of the same system. Let us consider Fig. A.3: the matrix M_3 is calculated as the product $M_2 \cdot M_1$, which represents respectively the propagation across a thin lens with focal length f and a free propagation for a distance d .

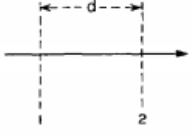
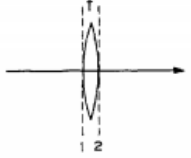
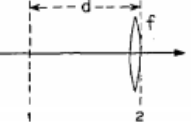
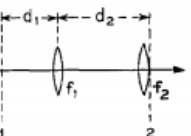
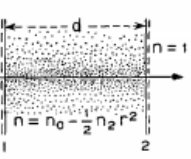
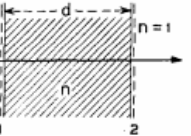
NO	OPTICAL SYSTEM	RAY TRANSFER MATRIX
1		$\begin{vmatrix} 1 & d \\ 0 & 1 \end{vmatrix}$
2		$\begin{vmatrix} 1 & 0 \\ -\frac{1}{f} & 1 \end{vmatrix}$
3		$\begin{vmatrix} 1 & d \\ -\frac{1}{f} & 1 - \frac{d}{f} \end{vmatrix}$
4		$\begin{vmatrix} 1 - \frac{d_2}{f_1} & d_1 + d_2 - \frac{d_1 d_2}{f_1} \\ -\frac{1}{f_1} - \frac{1}{f_2} + \frac{d_2}{f_1 f_2} & 1 - \frac{d_1}{f_1} - \frac{d_2}{f_2} + \frac{d_1 d_2}{f_1 f_2} \end{vmatrix}$
5		$\begin{vmatrix} \cos d \sqrt{\frac{n_2}{n_0}} & \frac{1}{\sqrt{n_0 n_2}} \sin d \sqrt{\frac{n_2}{n_0}} \\ -\sqrt{n_0 n_2} \sin d \sqrt{\frac{n_2}{n_0}} & \cos d \sqrt{\frac{n_2}{n_0}} \end{vmatrix}$
6		$\begin{vmatrix} 1 & d/n \\ 0 & 1 \end{vmatrix}$

Figure A.3. Transfer matrices for common optical systems [27].

The minor extension to this example consists in the addition of another free space region after the lens: this is a very common case and lead to a transfer matrix which have use in many applications. To calculate it we just need to multiply an M_1 type matrix with an M_2 type matrix and another M_1 . Naming d_1 and d_2 the distances before and after the lens, we have:

$$M = \begin{pmatrix} 1 & d_2 \\ 0 & 1 \end{pmatrix} \begin{pmatrix} 1 & 0 \\ -\frac{1}{f} & 1 \end{pmatrix} \begin{pmatrix} 1 & d_1 \\ 0 & 1 \end{pmatrix} = \begin{pmatrix} 1 - \frac{d_2}{f} & d_1 + d_2 - \frac{d_1 d_2}{f} \\ -\frac{1}{f} & 1 - \frac{d_1}{f} \end{pmatrix} \quad (\text{A.21})$$

A typical case of use of the matrix M is when the waists of the incoming and transformed beams lie at $z = 0$ and $z = d_1 + d_2$, hence both q and q' are purely imaginary and can be write as

$$\begin{aligned} q &= -i \frac{\pi w_0^2}{\lambda} \\ q' &= \frac{Aq + B}{Cq + D} = -i \frac{\pi w_0'^2}{\lambda} \end{aligned} \quad (\text{A.22})$$

where A , B , C and D are the element of the transfer matrix M , while w_0 and w_0' are the waists of the incoming and transformed beams. Separating the real and imaginary part of the last equality we can solve for the distances d_1 and d_2

$$\begin{aligned} d_1 &= f \pm \frac{w_0}{w_0'} \sqrt{f^2 - \tilde{f}^2} \\ d_2 &= f \pm \frac{w_0'}{w_0} \sqrt{f^2 - \tilde{f}^2} \end{aligned} \quad (\text{A.23})$$

with $\tilde{f} = (\pi/\lambda) w_0 w_0'$. It's important to note that, in order to obtain real solutions, we need $f \geq \tilde{f}$. In practice, Eq.A.23 can be used to determine the position of the lens when we need to transform the waist of the beam, for example to match the mode of a cavity or an optical fiber. In these cases we also need to make sure that the distance $d_1 + d_2$ do not exceed the total space we have for the mode matching, therefore it is not always possible to find suitable solutions.

Bibliography

- [1] AIKAWA, K., FRISCH, A., MARK, M., BAIER, S., RIETZLER, A., GRIMM, R., AND FERLAINO, F. Bose-einstein condensation of erbium. *Phys. Rev. Lett.*, **108** (2012), 210401. Available from: <https://link.aps.org/doi/10.1103/PhysRevLett.108.210401>, doi:10.1103/PhysRevLett.108.210401.
- [2] ANDERSON, M. H., ENSHER, J. R., MATTHEWS, M. R., WIEMAN, C. E., AND CORNELL, E. A. Observation of bose-einstein condensation in a dilute atomic vapor. *Science*, **269** (1995), 198. Available from: <https://science.sciencemag.org/content/269/5221/198>, arXiv:<https://science.sciencemag.org/content/269/5221/198.full.pdf>, doi:10.1126/science.269.5221.198.
- [3] ASHKIN, A. Optical trapping and manipulation of neutral particles using lasers. *Proceedings of the National Academy of Sciences*, **94** (1997), 4853. Available from: <https://www.pnas.org/content/94/10/4853>, arXiv:<https://www.pnas.org/content/94/10/4853.full.pdf>, doi:10.1073/pnas.94.10.4853.
- [4] BARANOV, M., DALMONTE, M., PUPILLO, G., AND ZOLLER, P. Condensed matter theory of dipolar quantum gases. *Chemical reviews*, **112** (2012), 5012. doi:10.1021/cr2003568.
- [5] BEAUFILS, Q., CHICIREANU, R., ZANON, T., LABURTHER-TOLRA, B., MARÉCHAL, E., VERNAC, L., KELLER, J.-C., AND GORCEIX, O. All-optical production of chromium bose-einstein condensates. *Phys. Rev. A*, **77** (2008), 061601. Available from: <https://link.aps.org/doi/10.1103/PhysRevA.77.061601>, doi:10.1103/PhysRevA.77.061601.
- [6] BISHOP, D. J. AND REPPY, J. D. Study of the superfluid transition in two-dimensional ^4He films. *Phys. Rev. Lett.*, **40** (1978), 1727. Available from: <https://link.aps.org/doi/10.1103/PhysRevLett.40.1727>, doi:10.1103/PhysRevLett.40.1727.
- [7] BLOCH, I., DALIBARD, J., AND ZWERGER, W. Many-body physics with ultra-cold gases. *Rev. Mod. Phys.*, **80** (2008), 885. Available from: <https://link.aps.org/doi/10.1103/RevModPhys.80.885>, doi:10.1103/RevModPhys.80.885.
- [8] BOHN, J., REY, A., AND YE, J. Cold molecules: Progress in quantum engineering of chemistry and quantum matter. *Science*, **357** (2017). doi:10.1126/science.aam6299.

- [9] BÖTTCHER, F., SCHMIDT, J.-N., WENZEL, M., HERTKORN, J., GUO, M., LANGEN, T., AND PFAU, T. Transient supersolid properties in an array of dipolar quantum droplets. *Phys. Rev. X*, **9** (2019), 011051. Available from: <https://link.aps.org/doi/10.1103/PhysRevX.9.011051>, doi:10.1103/PhysRevX.9.011051.
- [10] CAPOGROSSO-SANSONE, B., TREFZGER, C., LEWENSTEIN, M., ZOLLER, P., AND PUPILLO, G. Quantum phases of cold polar molecules in 2d optical lattices. *Physical review letters*, **104** (2010), 125301. doi:10.1103/PHYSREVLETT.104.125301.
- [11] CHIN, C., GRIMM, R., JULIENNE, P., AND TIESINGA, E. Feshbach resonances in ultracold gases. *Review of Modern Physics*, **82** (2010), 1225. doi:10.1103/RevModPhys.82.1225.
- [12] CHOMAZ, L., ET AL. Long-lived and transient supersolid behaviors in dipolar quantum gases. *Phys. Rev. X*, **9** (2019), 021012. Available from: <https://link.aps.org/doi/10.1103/PhysRevX.9.021012>, doi:10.1103/PhysRevX.9.021012.
- [13] COHEN-TANNOUDJI, C. AND GUÉRY ODELIN, D. *Advances in atomic physics: An overview* (2011). doi:10.1142/6631.
- [14] DAVIS, K. B., MEWES, M. O., ANDREWS, M. R., VAN DRUTEN, N. J., DURFEE, D. S., KURN, D. M., AND KETTERLE, W. Bose-einstein condensation in a gas of sodium atoms. *Phys. Rev. Lett.*, **75** (1995), 3969. Available from: <https://link.aps.org/doi/10.1103/PhysRevLett.75.3969>, doi:10.1103/PhysRevLett.75.3969.
- [15] DE MARCO, L., VALTOLINA, G., MATSUDA, K., TOBIAS, W., COVEY, J., AND YE, J. A degenerate fermi gas of polar molecules. *Science*, **363** (2019), 853. doi:10.1126/science.aau7230.
- [16] FILINOV, A., PROKOF'EV, N., AND BONITZ, M. Berezinskii-kosterlitz-thouless transition in two-dimensional dipole systems. *Physical review letters*, **105** (2010), 070401. doi:10.1103/PHYSREVLETT.105.070401.
- [17] FRISCH, A., ET AL. Ultracold dipolar molecules composed of strongly magnetic atoms. *Physical Review Letters*, **115** (2015). doi:10.1103/PhysRevLett.115.203201.
- [18] GAUBATZ, U., RUDECKI, P., SCHIEMANN, S., AND BERGMANN, K. Population transfer between molecular vibrational levels by stimulated raman scattering with partially overlapping laser fields. a new concept and experimental results. *The Journal of Chemical Physics*, **92** (1990), 5363. Available from: <https://doi.org/10.1063/1.458514>, arXiv:<https://doi.org/10.1063/1.458514>, doi:10.1063/1.458514.
- [19] GIOVANAZZI, S., GÖRLITZ, A., AND PFAU, T. Tuning the dipolar interaction in quantum gases. *Phys. Rev. Lett.*, **89** (2002), 130401. Avail-

- able from: <https://link.aps.org/doi/10.1103/PhysRevLett.89.130401>, doi:10.1103/PhysRevLett.89.130401.
- [20] GORAL, K., KOEHLER, T., GARDINER, S., TIESINGA, E., AND JULIENNE, P. Adiabatic association of ultracold molecules via magnetic field tunable interactions. *Journal of Physics B: Atomic, Molecular and Optical Physics*, **37** (2004). doi:10.1088/0953-4075/37/17/006.
- [21] GRIMM, R., WEIDEMÜLLER, M., AND OVCHINNIKOV, Y. B. Optical dipole traps for neutral atoms. **42** (2000), 95. Available from: <http://www.sciencedirect.com/science/article/pii/S1049250X0860186X>, doi: [https://doi.org/10.1016/S1049-250X\(08\)60186-X](https://doi.org/10.1016/S1049-250X(08)60186-X).
- [22] HADZIBABIC, Z. AND DALIBARD, J. Two-dimensional bose fluids: An atomic physics perspective. *Rivista del Nuovo Cimento*, **34** (2009). doi:10.1393/ncr/i2011-10066-3.
- [23] HODBY, E., THOMPSON, S., REGAL, C., GREINER, M., WILSON, A., JIN, D., CORNELL, E., AND WIEMAN, C. Production efficiency of ultracold feshbach molecules in bosonic and fermionic systems. *Physical review letters*, **94** (2005), 120402. doi:10.1103/PhysRevLett.94.120402.
- [24] HOROWITZ, P. AND HILL, W. *The art of electronics; 3rd ed.* Cambridge University Press, Cambridge (2015). Available from: <https://cds.cern.ch/record/1981307>.
- [25] HUANG, K. AND YANG, C. N. Quantum-mechanical many-body problem with hard-sphere interaction. *Phys. Rev.*, **105** (1957), 767. Available from: <https://link.aps.org/doi/10.1103/PhysRev.105.767>, doi:10.1103/PhysRev.105.767.
- [26] JULIENNE, P. S., HANNA, T. M., AND IDZIASZEK, Z. Universal ultracold collision rates for polar molecules of two alkali-metal atoms. *Phys. Chem. Chem. Phys.*, **13** (2011), 19114. Available from: <http://dx.doi.org/10.1039/C1CP21270B>, doi:10.1039/C1CP21270B.
- [27] KOGELNIK, H. AND LI, T. Laser beams and resonators. *Appl. Opt.*, **5** (1966), 1550. Available from: <http://ao.osa.org/abstract.cfm?URI=ao-5-10-1550>, doi:10.1364/AO.5.001550.
- [28] KOSTERLITZ, J. M. AND THOULESS, D. J. Ordering, metastability and phase transitions in two-dimensional systems. *Journal of Physics C: Solid State Physics*, **6** (1973), 1181. Available from: <https://doi.org/10.1088/2F0022-3719/2F6%2F7%2F010>, doi:10.1088/0022-3719/6/7/010.
- [29] KOTOCHIGOVA, S. AND PETROV, A. Anisotropy in the interaction of ultracold dysprosium. *Phys. Chem. Chem. Phys.*, **13** (2011), 19165. Available from: <http://dx.doi.org/10.1039/C1CP21175G>, doi:10.1039/C1CP21175G.
- [30] LAHAYE, T., MENOTTI, C., SANTOS, L., LEWENSTEIN, M., AND PFAU, T. The physics of dipolar bosonic quantum gases. *Reports on Progress in Physics*,

- 72 (2009), 126401. Available from: <https://doi.org/10.1088%2F0034-4885%2F72%2F12%2F126401>, doi:10.1088/0034-4885/72/12/126401.
- [31] LIMA, A. R. P. AND PELSTER, A. Beyond mean-field low-lying excitations of dipolar bose gases. *Phys. Rev. A*, **86** (2012), 063609. Available from: <https://link.aps.org/doi/10.1103/PhysRevA.86.063609>, doi:10.1103/PhysRevA.86.063609.
- [32] LU, M., BURDICK, N. Q., YOUN, S. H., AND LEV, B. L. Strongly dipolar bose-einstein condensate of dysprosium. *Phys. Rev. Lett.*, **107** (2011), 190401. Available from: <https://link.aps.org/doi/10.1103/PhysRevLett.107.190401>, doi:10.1103/PhysRevLett.107.190401.
- [33] LUCIONI, E., TANZI, L., FREGOSI, A., CATANI, J., GOZZINI, S., INGUSCIO, M., FIORETTI, A., GABBANINI, C., AND MODUGNO, G. Dysprosium dipolar bose-einstein condensate with broad feshbach resonances. *Phys. Rev. A*, **97** (2018), 060701. Available from: <https://link.aps.org/doi/10.1103/PhysRevA.97.060701>, doi:10.1103/PhysRevA.97.060701.
- [34] MAIER, T., FERRIER-BARBUT, I., KADAU, H., SCHMITT, M., WENZEL, M., WINK, C., PFAU, T., JACHYMSKI, K., AND JULIENNE, P. S. Broad universal feshbach resonances in the chaotic spectrum of dysprosium atoms. *Phys. Rev. A*, **92** (2015), 060702. Available from: <https://link.aps.org/doi/10.1103/PhysRevA.92.060702>, doi:10.1103/PhysRevA.92.060702.
- [35] MIAO, J., HOSTETTER, J., STRATIS, G., AND SAFFMAN, M. Magneto-optical trapping of holmium atoms. *Phys. Rev. A*, **89** (2014), 041401. Available from: <https://link.aps.org/doi/10.1103/PhysRevA.89.041401>, doi:10.1103/PhysRevA.89.041401.
- [36] MORSCH, O. AND OBERTHALER, M. Dynamics of bose-einstein condensates in optical lattices. *Rev. Mod. Phys.*, **78** (2006), 179. Available from: <https://link.aps.org/doi/10.1103/RevModPhys.78.179>, doi:10.1103/RevModPhys.78.179.
- [37] MÜLLER, S., BILLY, J., HENN, E. A. L., KADAU, H., GRIESMAIER, A., JONASLASINIO, M., SANTOS, L., AND PFAU, T. Stability of a dipolar bose-einstein condensate in a one-dimensional lattice. *Phys. Rev. A*, **84** (2011), 053601. Available from: <https://link.aps.org/doi/10.1103/PhysRevA.84.053601>, doi:10.1103/PhysRevA.84.053601.
- [38] NATALE, G., VAN BIJNEN, R. M. W., PATSCHEIDER, A., PETTER, D., MARK, M. J., CHOMAZ, L., AND FERLAINO, F. Excitation spectrum of a trapped dipolar supersolid and its experimental evidence. *Phys. Rev. Lett.*, **123** (2019), 050402. Available from: <https://link.aps.org/doi/10.1103/PhysRevLett.123.050402>, doi:10.1103/PhysRevLett.123.050402.
- [39] PETHICK, C. AND SMITH, H. *Bose-Einstein condensation in dilute gases*. Cambridge University Press (2002).

- [40] PETROV, A., TIESINGA, E., AND KOTOCHIGOVA, S. Anisotropy-induced feshbach resonances in a quantum dipolar gas of highly magnetic atoms. *Physical Review Letters*, **109** (2012). doi:[10.1103/PhysRevLett.109.103002](https://doi.org/10.1103/PhysRevLett.109.103002).
- [41] QUÉMÉNER, G., BOHN, J., PETROV, A., AND KOTOCHIGOVA, S. Universalities in ultracold reactions of alkali polar molecules. *Physical Review A*, **84** (2011). doi:[10.1103/PhysRevA.84.062703](https://doi.org/10.1103/PhysRevA.84.062703).
- [42] SANTOS, L. *Theory of dipolar gases*, vol. 94, pp. 231–271 (2012). ISBN 9780199661886. doi:[10.1093/acprof:oso/9780199661886.003.0006](https://doi.org/10.1093/acprof:oso/9780199661886.003.0006).
- [43] SAVARD, T. A., O'HARA, K. M., AND THOMAS, J. E. Laser-noise-induced heating in far-off resonance optical traps. *Phys. Rev. A*, **56** (1997), R1095. Available from: <https://link.aps.org/doi/10.1103/PhysRevA.56.R1095>, doi:[10.1103/PhysRevA.56.R1095](https://doi.org/10.1103/PhysRevA.56.R1095).
- [44] STUHLER, J., GRIESMAIER, A., KOCH, T., FATTORI, M., AND PFAU, T. Magnetostriction in a degenerate quantum gas. *Journal of Magnetism and Magnetic Materials*, **316** (2007), 429 . Proceedings of the Joint European Magnetic Symposia. Available from: <http://www.sciencedirect.com/science/article/pii/S0304885307004295>, doi:<https://doi.org/10.1016/j.jmmm.2007.03.097>.
- [45] TANZI, L., LUCIONI, E., FAMÀ, F., CATANI, J., FIORETTI, A., GABBANINI, C., BISSET, R. N., SANTOS, L., AND MODUGNO, G. Observation of a dipolar quantum gas with metastable supersolid properties. *Phys. Rev. Lett.*, **122** (2019), 130405. Available from: <https://link.aps.org/doi/10.1103/PhysRevLett.122.130405>, doi:[10.1103/PhysRevLett.122.130405](https://doi.org/10.1103/PhysRevLett.122.130405).
- [46] TANZI, L., MALOBERTI, J., BIAGIONI, G., FIORETTI, A., GABBANINI, C., AND MODUGNO, G. Evidence of superfluidity in a dipolar supersolid from non-classical rotational inertia. (2019). Available from: <https://arxiv.org/abs/1912.01910>.
- [47] TANZI, L., ROCCUZZO, S., LUCIONI, E., FAMÀ, F., FIORETTI, A., GABBANINI, C., MODUGNO, G., RECATI, A., AND STRINGARI, S. Supersolid symmetry breaking from compressional oscillations in a dipolar quantum gas. *Nature*, **574** (2019). doi:[10.1038/s41586-019-1568-6](https://doi.org/10.1038/s41586-019-1568-6).
- [48] TAYLOR, J. B. Magnetic moments of the alkali metal atoms. *Phys. Rev.*, **28** (1926), 576. Available from: <https://link.aps.org/doi/10.1103/PhysRev.28.576>, doi:[10.1103/PhysRev.28.576](https://doi.org/10.1103/PhysRev.28.576).
- [49] TICKNOR, C. Quasi-two-dimensional dipolar scattering. *Phys. Rev. A*, **81** (2010), 042708. Available from: <https://link.aps.org/doi/10.1103/PhysRevA.81.042708>, doi:[10.1103/PhysRevA.81.042708](https://doi.org/10.1103/PhysRevA.81.042708).
- [50] TICKNOR, C. Finite-temperature analysis of a quasi-two-dimensional dipolar gas. *Phys. Rev. A*, **85** (2012), 033629. Available from: <https://link.aps.org/doi/10.1103/PhysRevA.85.033629>, doi:[10.1103/PhysRevA.85.033629](https://doi.org/10.1103/PhysRevA.85.033629).

-
- [51] VALTOLINA, G., MATSUDA, K., TOBIAS, W., LI, J., MARCO, L., AND YE, J. Dipolar evaporation of reactive molecules to below the fermi temperature. (2020). Available from: <https://arxiv.org/abs/2007.12277v1>.
- [52] ZWIERLEIN, M., ABO-SHAER, J., SCHIROTZEK, A., SCHUNCK, C., AND KETTERLE, W. Vortices and superfluidity in a strongly interacting fermi gas. *Nature*, **435** (2005), 1047. [doi:10.1038/nature03858](https://doi.org/10.1038/nature03858).